Simulation and development of LFP cathodes

Érica Almeida
Master in Nanomaterials Science and Technology
Faculty of Sciences of the University of Porto
2024

Simulation and development of LFP cathodes

Érica Almeida

Dissertation/Internship/Project Report carried out as part of the Master in Nanomaterials Science and Technology

Department of Physics and Astronomy

2024

Supervisor
Prof. Dr. João Araújo, Associate Professor, Faculty of Science

External Host Supervisor
Rúben Pedroso, Researcher, CeNTI – Centre for Nanotechnology and Advanced Materials

“ You can’t crush ideas by suppressing them. You can only crush them by ignoring them. By refusing to think, refusing to change. ”

Ursula K. LeGuin, The Dispossessed: An Ambiguous Utopia

To the people who love me, who helped me more than they could ever know

Acknowledgements

The conclusion of this thesis represents a very important milestone in my life and I could not have done without the help, guidance and encouragement of many people.

I will now take this opportunity to express my deepest gratitude and sincere thanks to all those who made the conclusion of this long journey possible. I'd like to begin by thanking both my supervisors, Professor João Pedro Araújo and Rúben Pedroso for their invaluable help in the development of this work. To Professor João I'd like to express my sincere appreciation for the guidance and encouragement he never failed to show during these past few months. To Rúben I'd like to thank for the endless patience, availability and understanding he showed all throughout this project, alongside all the technical support he provided along the way.

To the whole team at CeNTI, who I had the privilege to work with for the duration of my thesis, I'd like to express my gratitude for the welcoming and friendly environment they created every day. In particular, I'd like to thank João Magalhães and Pedro Sampaio for their help and insight at several key points.

I'd also would like to thank Professor Eduardo Marques for his openness as director of the CNT Master's program and for his help in getting me the opportunity to work collaborate with CeNTI.

On a personal note, I'd like to express my heartfelt gratitude to my parents, for their unwavering support and love despite all the challenges life has thrown my way.

I would also like to say, from the bottom of my heart, a massive thank you to all my friends for their constant and overwhelming support, love and care they've shown me throughout the last few years. In particular, I'd like to thank Afonso Correia, Catarina Lemos, Sofia Silva (and her travelling Duck) and all the members of Kapangas and Whoo, who were always there for me from my first year until now.

To Jean Alves, for being the best friend anyone could have, for giving me a second home, for all the support, time and love she showed me through my roughest moments, I'd like to give the biggest "Thank You" I can put into words, which is still far from enough.

And last, but most important of all, I'd like to thank Liliana Ferreira for being my sun, and making my life immeasurably brighter with her presence.

Resumo

O aumento de procura de energia a nível global aliada à crise iminente provocada pelas alterações climáticas, tornou imperativa a investigação de métodos mais eficazes e amigos do ambiente para o armazenamento de energia. Devido a estes fatores, o investimento no desenvolvimento de baterias de iões de lítio aumentou exponencialmente. Parte dessa pesquisa concentra-se no desenvolvimento de modelos numéricos de células de baterias, permitindo a simulação e otimização de forma mais eficiente, barata e menos poluente. Este trabalho tem como foco o estudo e desenvolvimento de um modelo numérico de uma bateria de fosfato de ferro-lítio (LFP) com o objetivo de otimizar seu desempenho através da variação de vários parâmetros. O modelo referido foi construído e validado através do uso de uma bateria de óxido de cobalto de manganês de lítio-Níquel NMC. De seguida, realizou-se um estudo do impacto da espessura dos elétrodos positivos e negativos na sua capacidade. Os resultados dessas simulações foram então analisados tendo em conta os resultados experimentais e teóricos. As simulações refletem com precisão o que é observado experimentalmente e o que é esperado pelos modelos teóricos: a capacidade aumenta com o aumento da espessura dos elétrodos. Outras algumas observações mais subtis também foram feitas.

key: Baterias ião-lítio, cátodo LFP, Simulação numérica, P2D Newman

Abstract

The ever-increasing global demand for energy coupled with the impending crisis driven by climate change has made research into more efficient and environmentally conscious methods for energy storage an imperative.

Accordingly, Li-ion battery research as seen an exponential growth in investment. A considerable part of that research focuses on the development of numerical models of battery cells, allowing for the simulation and optimization in a more efficient, cheaper and less polluting way.

This work focuses on studying and developing a numerical model of a Lithium iron phosphate (LFP) battery with the purpose of optimizing its performance by through variation of its parameters.

The aforementioned model was built and validated using a lithium nickel manganese cobalt oxide (NMC) battery. Following that, a study of the impact of the thickness of the positive and negative electrodes on its capacity was conducted. The results of these simulations were then analysed in light of experimental results and theory. The simulations accurately reflect what is observed experimentally, and what is expected by theoretical models: the capacity increases with an increase in the thickness of the electrodes. Some more nuanced observations were also made.

Keywords: Lithium-ion batteries, LFP cathodes, Numerical simulation, P2D Newman

Table of Contents

List of Figures

List of Abbreviations

LFP Lithium Iron Phosphate

LIBs Lithium-ion Batteries

CITEVE Technological Center of the Textile and Clothing Industries of Portugal

CTIC Technological Center for Leather Discoveries

CEIIA Center for Excellence and Innovation in the Automotive Industry

CeNTI Center for Nanotechnology and Smart Material

P2D Newman Newman's Pseudo-Two Dimensional Model

PDAEs Partial Differential Algebraic Equations

PDEs Partial Differential Equations

PA Phytic Acid

CNTs Carbon Nanotubes

AB Acetylene Black

rGO reduced Graphene Oxide

CV Cyclic Voltametry

EIS Electrochemical Impedance Spectroscopy

[BMIm][N(CN)$_2$] 1-butyl-3-methylimidazolium dicyanamide

PHyA Hydrothermal-Alcohol Washing-Calcination Procedure Employing Phythic Acid

PVDF Polyvinlidene Fluoride

NC Nitrogen-doped Carbon

CTR Carbothermal Reduction

TR Three-Dimensional Thermal Runaway

LTO $Li_4T_{15}O_{12}$

CFD Computer Fluid Dynamics

LMO Lithium Manganese Oxide

LCO Lithium Cobalt Oxide

MSMD Multi-Scale Multi-Domain approach

OCP Open Circuit Potencial

SOC State of Charge

SOL State of Lithiation

UDF User Defined Function

Cs Solid-Phase Lithium Concentration

Ce Electrolyte-phase Lithium Concentration

VOF Volume Of Fraction

Ds Solid-Phase Diffusion Coefficient

OCP Open Circuit Potential

De Diffusion Coefficient in the Electrolyte

NMC Nickel Manganese Cobalt

1. Introduction

1.1. Motivation

Research into lithium-ion batteries (LIBs) has become increasingly important, both academically and for industry. This electrochemical energy storage technology has become ubiquitous in use for mobile devices and of growing use in electric vehicles. Indeed, modest estimations point to 11% to 28% of the automobile market being electric-powered vehicles by 2040 [1] while more optimist projections claim complete market dominance by 2050 [2]. Naturally, with such wide use and demand, improvements to the technology are continually sought out after. Thus far, production costs have fallen at a fast pace, with steady improvements in power and energy density [3].

The choice of cathode material in lithium-ion batteries has a large impact on its overall performance. One such cathode material is lithium iron phosphate, or LFP, which has seen growing adoption and shows great potential. The characteristics of the cathode, such as morphology, also have a major impact in its performance. However, optimization and manufacturing of LFP batteries with different characteristics can be expensive, time-consuming and difficult from a technical standpoint. To make such optimization cheaper and faster, there have been an increase in research dedicated to numerical simulations of Li-ion batteries with precisely such a goal in recent years. Numerical simulations allow for a way to test different potential battery electrode materials and designs without having to manufacture them, as long as the parameters required for the simulation model are known a-priori or have the possibility of being estimated.

Although most of the aforementioned research focuses on thermal analysis and optimization, there are also works that deal with the optimization of the electrochemical characteristics of the batteries. Given this context, this project aims to apply an existing simulation model, to reliably simulate a lithium-ion battery with an LFP cathode, and investigate possible avenues of optimization for some of its parameters, thus allowing for a more efficient, faster and cheaper production of high-performance LFP batteries.

1.2. Project objectives

This thesis has as its main goals to develop a reliable simulation model of an LFP coin-cell battery and to use it to study possible parameters for optimization. To achieve this, it is planned to:

- Conduct research into LFP batteries, in particular, LFP cathodes, and become familiar with their characteristics.
- Investigate different Li-ion battery simulation models, choose the most adequate one for the needs of this project and become proficient in its use.
- Develop an LFP battery model and validate it with experimental data.
- Investigate potential parameters for optimization of the simulated LFP battery.
- Obtain and analyse the chosen optimization parameters for the model

1.3. CeNTI- Center for Nanotechnology and Smart Materials

CeNTI, the Center for Nanotechnology and Smart Material, is Portuguese R&D institute specializing in research and development for various industrial sectors. It was born of a collaboration of several different institutes, namely, the University of Porto, the University of Aveiro, the University of Minho, the Technological Center of the Textile and Clothing Industries of Portugal (CITEVE), and the Technological Center for Leather Discoveries (CTIC) with a small involvement of the Center for Excellence and Innovation in the Automotive Industry (CEIIA). Employing almost 200 researchers as of 2024, CeNti has an extensive repertoire of projects (20 with European funding, 111 with national funding, and 170 in partnership with industrial companies) and several patents (67 active applications and 35 granted ones).

CeNTI's work spans the development of several areas, such as new materials, new coatings, and new technologies for automobile, aeronautical, construction, architecture, intelligent spaces, health, protection and well-being, and industries, including textiles, polymers, leather, paper, glass, ceramics, natural stone, concrete, cork, wood, etc. More recently, the center has been involved in several projects related to new forms of energy production and storage, mainly renewable sources of energy, and battery development [4].

2. Theory

LIBs have become integral parts of modern life, being used extensively in mobile devices and, with more recent advancements, being a practical solution to power electric vehicles.

Naturally, with such wide use and demand, research into this energy storage technology has become increasingly important and improvements are continually sought after. The choice of cathode material in lithium-ion batteries has a large impact on its overall performance. One such cathode material is LFP which has seen growing adoption and shows great potential. The characteristics of the cathode, such as morphology, also have a major impact in its performance. However, manufacturing and optimization of LFP cathodes with different characteristics can be expensive, time-consuming and difficult from a technical standpoint. Given this context, the goal with this dissertation is to create a reliable simulation model of a lithium-ion battery with an LFP cathode, and subsequent optimization of some of its parameters, thus allowing for a more efficient, faster and cheaper production of high-performance LFP batteries.

2.1. Theoretical fundamentals of Lithium-ion Batteries

The first electrochemical cells are believed to have been the product of the work of two Italian scientists, Alessandro Volta and Luigi Galvani in the late eighteen-hundreds in the Universities of Pavia and Bologna, respectively [5].

However, the history of modern LIBs begins in the 1960s, with the development of primary-type batteries to meet demands of consumer electronics, mostly in the form of coin-cells. Secondary-type batteries, which are rechargeable, were developed later, in the late 1970s to early 1980s. Practical commercial application only occurs over a decade later in 1991 [6].

Lithium-ion batteries have a layered structure, consisting of two major electrodes, a positive one, the cathode, a negative one, the anode and a porous membrane in between them called the separator. The region containing these components is often called the electrolyte. The outside layer of the structure is composed of the positive and negative current collectors who connect to the cathode and anode, respectively. A diagram representing the usual structure of a modern LFP battery can be seen on 2.1. The cathodes are generally composed of lithium metal oxides, these kinds of materials store lithium ions

in their layered structured through electrochemical intercalation in lattice sites. Anodes, on the other hand, are generally made from compounds of different types of carbons. The electrolyte is the medium that ensures the transfer of ions between the electrodes, with the separator creating a barrier between the electrodes, blocking electron flow across the interior of the system.

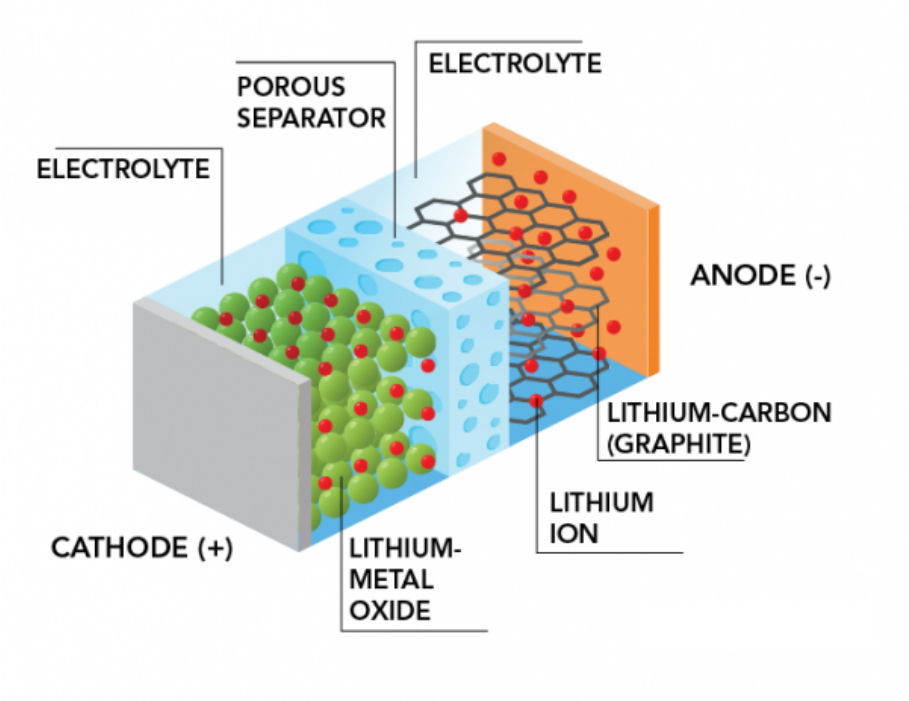

Figure 2.1: Diagram of the structure of a typical LFP battery [7].

Like all batteries, LIBs are devices that produce electrical energy from the conversion of stored chemical energy. During the discharge process, energy is generated by the movement of lithium ions across the electrolyte from the negative to the positive electrode. Electrons flow occurs in the reverse direction through the external circuit. Charging is the inverse process, a current is established in the external circuit, with electrons flowing to the negative electrode and staying there. The positive electrode lets go of several of its Li ions, which move towards the negative electrode, combining with the electrons present. The number of ions capable of moving over is determined by the battery capacity, and when no more ions can move, the charging process is complete and the battery is charged.

2.2. LFP cathodes

Lithium iron phosphate has an olivine crystalline structure, composed of three distinct components: two octahedrons, FeO_6 and LiO_6, and one tetrahedron PO_4 [8].

The FeO_6 octahedra link together by their corners, while the LiO_6 ones are linked by shared edges. In the layer between these two, the tetrahedra are located [9]. The LFP structure described can be seen in figure 2.2.

This morphology results in the formation of narrow pathways for the Li-ion diffusion, in the form of one-dimensional ”holes”. In contrast, other cathode materials possess two, or even three-dimensional diffusion channels[8, 10, 11]. This fact limits the diffusion of Li^+ ions in both charging and discharging, and is also responsible for the low electric conductivity of $LiFePO_4$ [12]. Furthermore, it makes $LiFePO_4$ performance highly susceptible to structural defects [13, 14].

Taking into account the limitations of $LiFePO_4$, extensive research as been conducted to overcome them and improve its performance. Four main approaches can be found in the literature [8]: morphology and particle size control, surface modification by coating with carbon, cation doping and by introduction of additives pre-lithiation. A large amount of research was compiled regarding some of these topics. Besides particle size, the simulation model used is not capable of taking into account such parameters. Regardless, an understanding of the effects of these modifications is of interest, thus a brief exploration of each will be done in chapter 3.

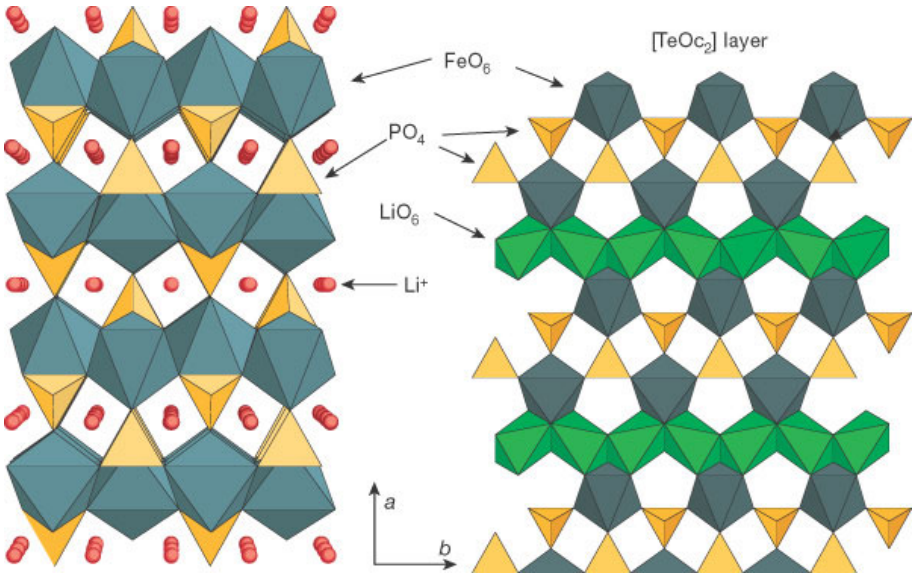

Figure 2.2: Crystal structure of olivine LiFePO4 projected along the [001] plane [9].

2.3. Choice of model

Many Li-ion battery models exist. Different models aim to describe a set of different physical characteristics of batteries. Extensive literature on the topic as been published.

Battery models can broadly be classified into two different categories: Physical and empirical * [15].

Both types aim to simulate Li-ion battery behaviour but use different approaches. Empirical models are developed based on experimental data obtained from a specific cell. Parameters are determined from said experimental data, and this process can be quite expensive in terms of cost, effort and time. Additionally, models developed are specific to a given system, and cannot be applied to simulate other batteries with any degree of accuracy. However, they're easy to solve with a low computational cost. Physical models, on the other hand, are created from the ground-up from fundamental physical principles. This allows for a deeper understanding of the mechanisms involved and a greater accuracy in the resulting predictions at the cost of being much more computational-intensive to run. Empirical models are often used for control and prediction in real time settings, while Physical models are used for deeper analysis in a research context. Given the needs of this work, the model used will be the Newman's pseudo-two dimensional model (P2D Newman), which is the most broadly used physical model for simulation of lithium-ion batteries.

2.4. P2D Newman

P2D Newman model was first introduced in 1993 [16] by Mark Doyler, Thomas Fuller and John Newman †. In subsequent years, it was used and expanded upon by the authors and many other scientists [17–21]. The P2D model integrates porous-electrode theory, concentrated solution theory and variations in ionic and electronic diffusivities conductivities to derive its equations [22]. Porous-electrode theory was developed in an earlier work by Tiedemann and Newman, using a macroscopic approach for the study of batteries [23]. Due to challenges related to the geometry, the equations derived were based on continuous functions and average quantities.

A schematic of the anatomy of a Li-ion battery as represented in Newman's model can be seen in fig. 2.3. The electrodes are composed of the electrolyte solution and the active materials. The active materials are treated as a solid phase and modelled as a matrix of spherical particles of equal size. The electrolyte phase is present in both electrodes and the separator and is continuous across all three regions. It is of note that, within the model, the solid and the electrolyte phase are considered as overlapping mediums,

*There are several nomenclatures used in the literature. Some authors refer to these categories as electrochemical and semi-empirically, respectively.

†It is also occasionally referred to as the DNF model, based on the initials of the researchers.

with no structure at their interface. The current collectors are passive zones in which no equations are solved.

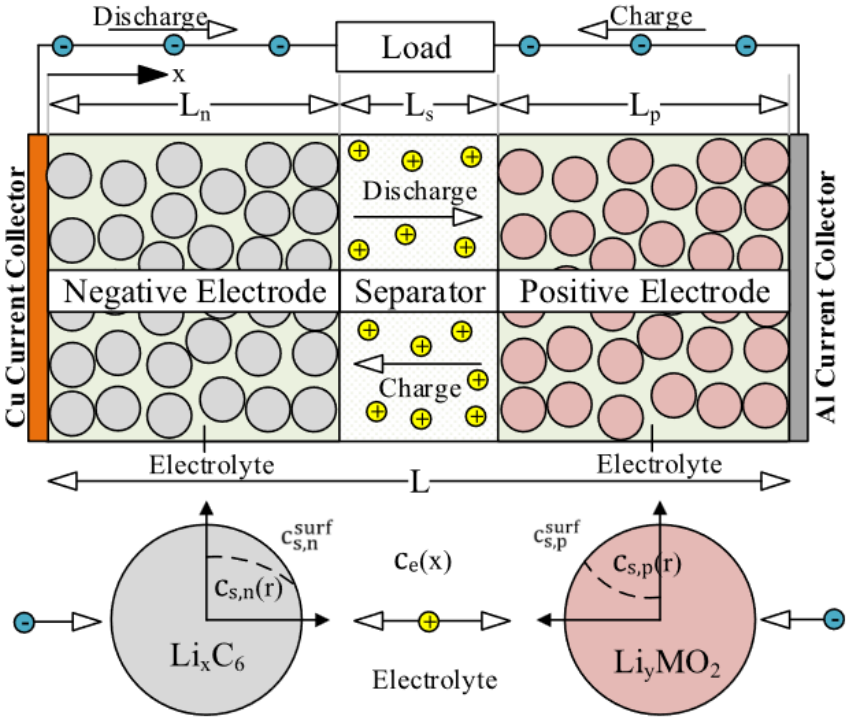

Figure 2.3: Representation of a Li-ion battery within the P2D model. With the electrode domain above and the particle domain below.

2.4.1 Governing equations of the P2D model

The governing equations of the P2D model are presented below, alongside a brief description of their key features [22].

To model the transport of lithium in the solid phase, porous electrode theory is used. The concentration of Li^+ in the solid phase can be described using Fick's laws of diffusion as:

$$\frac{\partial c_{s,k}(x,r,t)}{\partial t} = \frac{D_{s,k}}{r^2}\frac{\partial}{\partial r}\left(r^2\frac{\partial c_{s,k}(x,r,t)}{\partial r}\right) \tag{2.1}$$

Where k can be either $k = p$ or $k = n$, denoting the positive and negative electrode, respectively.

The concentration of Li^+ in the electrolyte phase can be given by:

$$\epsilon_k\frac{\partial c_{e,k}(x,t)}{\partial t} = \frac{\partial}{\partial x}\left(D_{\text{eff},k}\frac{\partial c_{e,k}(x,t)}{\partial x}\right) + a_k(1-t_+)J_k(x,t) \tag{2.2}$$

This equation reflects the fact that the electrolyte phase changes in accordance with changes in the gradient diffusive flow of the lithium ions.

The conservation of charge of both electrodes in the solid phase is described by Ohm's law:

$$\sigma_{\text{eff},k}\frac{\partial^2\Phi_{s,k}(x,t)}{\partial x^2} = a_k F J_k(x,t) \tag{2.3}$$

Combining Ohm's and Kirchhoff's laws yields the conservation of charge in the electrolyte phase:

$$-\sigma_{eff,k}\frac{\partial\Phi_{s,k}(x,t)}{\partial x} - \kappa_{eff,k}\frac{\partial\Phi_{e,k}(x,t)}{\partial x} + \frac{2\kappa_{eff,k}RT}{F}(1-t_+)\frac{\partial \ln c_{e,k}}{\partial x} = I \tag{2.4}$$

It is useful to note that the effective electronic conductivity can be described as a function of the electrode's porosity:

$$\sigma_{\text{eff},k} = \sigma_k\left(1-\epsilon_k-\epsilon_{\text{f},k}\right) \tag{2.5}$$

Butler-Volmer kinetics are used to describe the relationship between the current density, concentrations and the over-potential between the two electrodes and the electrolyte [24]. In particular, the Butler-Volmer equation is applied to calculate the current density *, which translates the flux of Li^+ ions across the pore wall in the electrodes:

$$J_k(x,t) = K_k(c_{\text{s},k,\max}-c_{\text{s},k,\text{surf}})^{0.5}(c_{\text{s},k,\text{surf}})^{0.5}c_{\text{e},k}^{0.5}(x,t)\times\left[\exp\left(\frac{0.5F}{RT}\mu_{s,k}(x,t)\right)-\exp\left(-\frac{0.5F}{RT}\mu_{s,k}(x,t)\right)\right] \tag{2.6}$$

The aforementioned over-potential can be expressed as:

$$\mu_{s,k}(x,t) = \Phi_{s,k}(x,t) - \Phi_{e,k}(x,t) - U_k(\theta_k(x,t)) \tag{2.7}$$

Where the open-circuit potential equations for both electrodes, must be curve-fitted from experimental data. The voltage of the cell can be calculated explicitly through the expression:

*Also known as molar flux.

$$V_{cell}(t) = \Phi_{s,k}(0,t) - \Phi_{s,k}(L,t) \tag{2.8}$$

Overall, the equations 2.1, 2.2, 2.3, 2.4, 2.6 and 2.7, alongside the open-circuit potential equations, which are dependent on the chosen electrodes, must be solved. Thus, the model is a system with 14 unknowns and 14 nonlinear partial differential algebraic equations (PDAEs).

2.4.2 Limitations of the P2D model

Despite its high accuracy and wide use for Li-ion battery simulation, the P2D model has several limitations that are important to be aware of. The six most important of which will be detailed in the following paragraphs.

One such limitation is its computational complexity. Due to the number of partial differential equations (PDEs) that are required to be solved by the model, it becomes very computationally expensive, even when compared to other physical models. This is due to the high level of discretization necessary to simulate the diffusion dynamics in the electrolyte and solid phases. This can be circumvented by methods such as lumped or single-particle models; however, these are not completely faithful as they can miss key phenomena [25]. The second limitation pertains to the lack of ageing and degradation mechanisms. Since these impact battery life and safety, this factor makes the P2D model inadequate for long-term use analysis. Attempts to eliminate this weakness include incorporating these mechanisms into the model, this however increases the complexity and the already high computational cost. To achieve this experimental data is required, which is not always available, making this solution even more unreliable.

The assumption of homogeneity restrains the capabilities of this method as well, since the electrodes present very non-uniform characteristics, leading to degradation and performance issues the model cannot capture. This could be added to the model, leading once again to a significant increase in the already high computational cost. This downside specifically affects large format batteries since these irregularities can have more catastrophic consequences than in small format batteries.

Another assumption made by the P2D model is isothermal conditions. The electrodes experience great spatial temperature variations, especially when under high current or fast

charging/discharging conditions. The lack of accountability for these factors can deteriorate the performance or safety conditions of the battery. Adding improved thermal models has been proven challenging since precise parameterization is hard to obtain. Moreover, the P2D is less than ideal when it comes to extreme conditions such as extreme temperatures, high discharge rates, or low states of charge. Other models can be used for these situations that, once again, require higher computational power.

Additionally, this is a model that relies heavily on the accuracy of input parameters, many of which are difficult to measure experimentally leading to uncertainty in the model's output, especially when scaling from laboratory cells to commercial batteries. The P2D model also assumes that the parameters are constant throughout the battery's life which is false for most cases. Finally, the calibration of the model requires very detailed characterization techniques which, due to the stage of development, may not be feasible for all battery systems.

3. State of the art

3.1. Recent improvements for LFP cathodes

As stated in the previous chapter, in this section a brief overview of the state-of-the-art research into LFP cathode will be presented, covering particle size control and morphology, surface modification and element doping. After that, an overview of recent research conducted in battery simulation will be reported. Much of the research presented won't be of simulation of LFP cathodes specifically, nor of simulations with the same goal, however, the works discussed are still of interest, showing what is possible to achieve using these numerical methods.

3.1.1 Particle size control and Morphology

It has been shown that diffusion of Li ions in $LiFePO_4$ is anisotropic within its structure, with it only occurring along the [010] direction [26], which in agreement with the theoretical calculations of Islam et al. [27], which state that precisely this direction possesses a much lower activation energy for Li^+ diffusion.

Accordingly, efforts have been made in optimizing the diffusion pathways in this direction through morphology and particle size control.

For instance, it has been found by Su et al. [28] that reducing LFP particles to the microscale, with nanoscale sized building blocks, improves tap density, rate capacity and cycling performance. The mechanisms proposed to explain such improvement are the reduction of the pathway length for ion diffusion inside the 1-dimensional channel and the reduction of local, structure-destroying reactions caused by high Li^+ ion flux that occurs when operating at a high charge/discharge rate. Further reducing the particle size to the nanoscale, although improving the high power density, has negative repercussions on the volumetric energy density, caused by the increased surface area and its need for higher amount of binders, which also negatively affect cycling life. The synthesis method used to obtain the nano/microspheres was a standard hydrothermal method with the addition of a novel phosphorus source, Phytic acid (PA).

Chen et al. [29] described similar results by synthesizing porous micrometer sized, starfish-like nanostructured $LiFePO_4$ with excellent cycle stability, high tap density and high rate capacity, via a standard solvothermal approach using triethylamine.

Several groups have produced hollow LFP nanoparticles via solvothermal synthesis [30, 31]. The hollow structure helps to combat the problems inherent with size reduction to the nanoscale by providing void space to accommodate the volume change of the cell and the consequent stress caused by the charge/discharge process, while also providing shorter pathways for Li^+ diffusion and improving fatigue resistance, increasing the stability of the electrode [30]. Zhen et al. [30] reported the synthesis of hollow $LiFePO_4$ nanoparticles with excellent electrochemical properties, in particular a discharge capacity of $165.2\ \mathrm{mAh/g}$ at $0.1\ \mathrm{C}$ and $120.9\ \mathrm{mAh/g}$ at $10\ \mathrm{C}$ and a capacity retention rate of above 98 % after 50 cycles. In a similar work, Yang et al. [31] reported hollow microspherical LFP material with a polycrystalline structure. The sphere produced were of uniform size of around $1\ \bar{}\mathrm{m}$ consisted of aggregated nanoparticles. The measured charge/discharge capacities were high at different discharge rates, for instance, $158\ \mathrm{mAh/g}$ at $0.1\ \mathrm{C}$ and $101\ \mathrm{mAh/g}$ at $20\ \mathrm{C}$, which maintained 80 % of its capacity after 2000 cycles.

Synthesis of single-crystalline, [010]-oriented LFP nanosheets has been reported by Zhao et al. [32]. The particles were synthesised via standard solvothermal synthesis and demonstrated high capacities, $151\ \mathrm{mAh/g}$ at $0.5\ \mathrm{C}$ and $140\ \mathrm{mAh/g}$ at $1\ \mathrm{C}$. This high performance was attributed to the low-energy barrier for Li^+ diffusion on the [010] direction. Seemingly in agreement, Huang et al. [33] demonstrated in their work studying LFP particles with different orientations caused by pH differences in the solvothermal synthesis process, that samples with [100] direction show very poor electrochemical performance, as low as $70\ \mathrm{mAh/g}$ at $0.5\ \mathrm{C}$ and $15\ \mathrm{mAh/g}$ at $10\ \mathrm{C}$. However, another, more recent work by Li et al. [34], presents high performance, [100]-oriented LFP nanoflakes, with $164\ \mathrm{mAh/g}$ at $0.1\ \mathrm{C}$ and $122\ \mathrm{mAh/g}$ at $20\ \mathrm{C}$, with a high cycle stability of 90 % at $10\ \mathrm{C}$ after 1000 cycles, putting in question the idea that diffusion across the [010] is the only viable one for LFP particles.

The change in morphology of LFP particles and its impact in electrochemical performance due to change in the precursor concentration was studied by Huang et al.[35]. Through facile solvothermal synthesis, the concentration of the precursor solution was increased, from $0.15\ \mathrm{M}$ to $0.90\ \mathrm{M}$. It was noted that the morphology of the particles changed progressively from a spindle-shape, to a plate-type to finally a hierarchical club-shaped structure. Other parameters, such as temperature and exposure time were varied, at a concentration of $0.30\ \mathrm{M}$, and no change in structure was observed, showing that precursor concentration plays a relevant role in morphology control. The optimal precursor concentration was determined to be $0.30\ \mathrm{M}$, resulting in plate-type $LiFePo_4$ with high capacity rate of 140.8

$\mathrm{mAh/g}$ at 10 C, alongside excellent cycling performance and rate (95% capacity after 1000 cycles). The mechanism proposed to explain and determine the change in morphology was the restriction that attached nuclei impose on the structure and the adsorption of anions on the [100] direction. The proposed mechanism is coherent with the fact that the predominantly exposed facet was in that same plane.

Similarly, Ma et al. [36] reported a change in morphology of LFP particles with solvent composition using a solvothermal synthesis strategy. With increasing water content in the solvent, the morphology $LiFePO_4$ gradually changed from nanoplates into a hexagonal prism nanorods shape (ratio of glycerol-to-water of 1:1). The prism nanorods particles were shown to have superior electrochemical properties when compared to other morphologies, $163.8\ \mathrm{mAh/g}$ at 0.2 C and $75\ \mathrm{mAh/g}$ at 20 C, a high discharge rate, with good stability at both rates. The proposed explanations for the results were shorter diffusion length for the Li^+ ions on the [010] direction and the moderate size of the particles. Additionally, it was noted that the prism nanorod's morphology is similar in structure to the equilibrium shape of the lithium iron phosphate crystal.

The impact of temperature and exposure time during synthesis on the electrochemical performance of LFP has been reported [37, 38]. It was found by Xiuqin et al. [37] that temperature has a great impact on crystallinity of $LiFePO_4$ as well as the morphology, with higher temperatures, above 160ºC, and a fast-heating apparatus being ideal for obtaining a high performance sample through a hydrothermal process. Huang et al. [38] reached similar conclusions by synthesizing LFP particles with a solvothermal process, with samples prepared at 180ºC and with extensive exposure (4 hours) being stable and having no detectable structural defects related to lithium vacancies and antisite defects. These defects can block Li^+ ion diffusion pathways and reduce electrochemical performance.

3.1.2 Surface Modification and Coating

One of the limitations of $LiFePO_4$ compared to other cathode materials is its low electronic conductivity. Good conductivity is an important factor for obtaining high performing cathodes for lithium-ion batteries. Because of this, improving the surface conductivity of LFP particles as been a focus of groups working with this material.

Coating of LFP particles appears as a reliable method of improving surface electric conductivity and material performance at high rates [39] while, simultaneously, providing additional benefits, such as preventing direct contact of electrolytes with the active material,

consequently preventing it from participating in the chemical reaction, and surface degradation [40].

Among the researched alternatives, carbon coating is, by far, the most common method of coating of LFP particles. Carbon is so popular due to being low cost, highly stable and having high electronic conductivity. Carbon coating has been shown to play a role as a reducing agent, preventing the undesirable oxidation of Fe^{2+} [41]. As discussed before, reducing the length of the diffusion paths for ionic diffusion is desirable, and carbon contributes to that by acting as nucleating agent and, thus, suppressing the growth of LFP grains within the cathode material [42]. Additionally, carbon addition has been shown to be able to control particle size, structure and the growth mechanism during synthesis [43].

When performing carbon-coating on LFP particles, several parameters affect performance. The more relevant ones are: the carbon source used (organic, inorganic or a mixture), the extent of the graphitization, the porosity of the coating layer and its thickness.

The carbon source strongly influences the properties of the coating layer [44–46]. Inorganic carbon compounds such as graphene, carbon nanotubes (CNTs), acetylene black (AB) and super P offer a great control over the carbon quality, meaning, among other factors, the graphitization degree and electric conductivity of the resulting layer. However, the quality of the layer structure is usually limited, with thickness, homogeneity and coverage being hard to control. In contrast, organic sources such as glucose, lactose and citric acid mirror the advantages and disadvantages of the inorganic precursors, allowing for easy and uniform coating layers and structure but providing limited carbon quality. Additionally, organic sources are easily transformed in carbon during pyrolysis. Due to these properties, using a mix of both types appears as a promising avenue to produce high performance carbon-coated LFP particles. Research into this process is difficult, as finding the optimal ratio of organic/inorganic precursor can be challenging, as it can vary with the chemical structure of the electrode and its geometry, namely shape and size, even while using the same sources [47–49].

Using the idea of utilizing both organic and inorganic carbon sources for coating, Ding et al. [50] synthesized, via a solvothermal process and a posterior heat treatment, an LFP-carbon composite consisting of a nanoscale continuous coating of pyrolyzed conductive carbon interconnected with graphene sheets. The performance obtained was high across discharge rates, with $170\ \mathrm{mAh/g}$ at $1\ \mathrm{C}$ and $104\ \mathrm{mAh/g}$ at $50\ \mathrm{C}$. This performance was

attributed to the obtained structure, which was hierarchical, composed of two interconnected and complementary carbon transport networks. The primary network served as an extended current conductor and was constituted by overlapping graphene sheets. The secondary network served as an enabler of access, allowing for rapid charge extraction and injection to the nanocrystal surfaces, being a continuous nanoscale carbon surface. This secondary network increased the cycle stability of the $LiFePO_4$, by preventing the corrosion of the electrolytes caused by the nanocrystals, and improved rate performance.

Similarly, Jiang et al. [51] fabricated an LFP composite of carbon and reduced graphene oxide (rGO) via a simple solvothermal process and post treatment. The authors also synthesized a simple carbon-coated LFP sample to have a point of comparison for electrochemical performance of the LFP@C/rGO composite. The results obtained were remarkable, with the LFP@C/rGO composite outperforming the LFP@C sample, with discharge capacities of $148.3\ \mathrm{mAh/g}$ at $1\ \mathrm{C}$ and $129\ \mathrm{mAh/g}$ at $20\ \mathrm{C}$. It was also noted that the capacity fading after 200 cycles was null. The improved performance over the LFP@C sample was attributed to synergistic effects due to the three-dimensional conductive network formed by the carbon layer and the rGO, which effectively accelerated both Li^+ and electron migration. This attribution was further supported by cyclic voltammetry (CV) and Electrochemical Impedance spectroscopy (EIS) measurements, which pointed to improved Li^+ diffusion kinetics caused by coupling between rGO and the carbon layer.

In contrast, Oh et al. [52] explored the use of two complementary inorganic sources and reported a dual layer coating strategy for LFP material utilizing reduced graphene oxide and N-doped carbon. The N-doped carbon was derived from polydopamine and the dual carbon layers were synthesized by a one-pot polymerization process followed by thermal treatment. The produced composite was shown to have a high discharge capacity of $115\ \mathrm{mAh/g}$ at $10\ \mathrm{C}$ and $98\ \mathrm{mAh/g}$ at $30\ \mathrm{C}$ with a capacity retention of 96.18% after 700 cycles. The excellent long-term cycling stability and high rate performance were attributed to several factors. Firstly, the multifunctional role of polydopamine which was responsible for the enhanced electric conductivity due to the uniform N-doped carbon coating of each particle, the small particle size which induced fast lithium-ion diffusion and the well-connected electron pathways which reduced the contact resistance between the $LiFePO_4$ particles and the rGO. Secondly, the interconnected nature of the rGO strcuture who induced fast electron transport, and, finally, the synergistic effects between the two layers, as can be deduced for the improved electrochemical properties of the dual layer composite when compared with LFP sample coated with only reduced graphene oxide or

only N-doped carbon.

In their work to determine the effect of different carbon sources on coating quality and thickness, Meng at al. [49] produced LFP samples coated with two different precursors: glucose and 1-butyl-3-methylimidazolium dicyanamide ([BMIm][N(CN)$_2$]). Structure characterization techniques indicate that the carbon source used has great influence on the coating film, while having no effect on the LFP particles themselves. It was found that ([BMIm][N(CN)$_2$]) source creates a unique structure described as an ultrathin ($1-2\ \mathrm{nm}$), highly graphitized and uniform carbon films which led to a superior electrochemical performance when compared to the sample coated with glucose. In particular, ([BMIm][N(CN)$_2$]) was reported to have a superior electrode reaction reversibility, specific discharge capacity of $143.6\ \mathrm{mAh/g}$ at $1\ \mathrm{C}$ and a capacity retention of $160.6\ \mathrm{mAh/g}$ at $0.1\ \mathrm{C}$ with a decay after 50 cycles of only 1.47%.

In a work studying the effects of carbon coating on the crystal orientation of LFP along with its impact on electrochemical performance, Wang et al.[53] synthesized, through a hydrothermal method, nanocrystalline $LiFePO_4$ in which the (010) face is predominantly exposed. Several samples with increasing carbon contents (from 1.65 to $6\ \mathrm{wt\%}$) were prepared and a marked change in preferred orientation was noted. With the increase in carbon content used in synthesis, the preferential orientation changed from (010) to (100). This resulted in a lowering of the electrochemical performance, which was confirmed due to the as the optimal results being obtained for a (010)-preferred orientation sample at $1.65\mathrm{wt\%}$, with a discharge capacity of $162\ \mathrm{mAh/g}$ at $0.1\ \mathrm{C}$ and discharge efficiency of 95.4% at that same rate. These findings are in agreement with the idea that this orientation is the one with the lowest insertion and extraction potential, and shorter length pathways for Li^+ diffusion, allowing for faster ion movement.

Guan et al. [54] reported the synthesis of a composite of LFP, activated carbon and graphene, by a facile solvothermal method. This composite was shown to have remarkable electrochemical properties, namely, a very high capacity of $66\ \mathrm{mAh/g}$ at the very high discharge rate of $100\ \mathrm{C}$, with a high cycling stability of 82% after 3000 cycles, which points to a high power density. These results were attributed to abundant Li-ion diffusing pathways and fast electron transfer arising from the porous structure of the AC and the conductive graphene network.

One of the limitations of carbon coating is the low tap density associated with coating and the high processing cost, which is often causes reduced energy density in full battery cells.

In an effort to avoid such downsides, Cao et al. [55] produced an LFP composite microspheres constituted by co-modified graphene and glucose-derived carbon by an in situ one-pot solvothermal synthesis followed by an annealing process. These microspheres, with a diameter in the range of $5 - 12$ μm are self-assembled by carbon coated LFP nanoparticles with embedded graphene sheets and possess a unique three-dimensional morphology. This composite delivered impressive electrochemical properties, with a high reversible capacity of 163.7 $\mathrm{mAh/g}$ at 0.1 C, good rate capabilities of $137.3\mathrm{mAh/g}$ at 1 C, 107.1 $\mathrm{mAh/g}$ at 5 C and 94.9 $\mathrm{mAh/g}$ at 10 C. It was proposed that the unique porous structure, high degree of graphitization and overall uniform thickness of both layers was responsible for these remarkable properties.

It is well known that the theoretical limit for the specific capacity of $LiFePO_4$ is 170 $\mathrm{mAh/g}$ and, typically, the capacities obtained in commercially available carbon-coated LFP cathodes are around $120 - 160$ $\mathrm{mAh/g}$. In 2012, Hu et al. [56] reported a carbon-coated LFP cathode capable of reaching a specific capacity of 208 $\mathrm{mAh/g}$, vastly outdoing the theoretical limit. Commercial available LFP particles, with a particle diameter of around 200 nm, were coated with an amorphous carbon layer, and, following that, the particles were coated again with electrochemically exfoliated few-layer graphene. This last graphene coating was proposed as the explanation for the excess capacity over the theoretical limit, due to the reversible reduction-oxidation reaction that occurs between the Li^+ ions of the electrolyte and the exfoliated graphene flakes, as these flakes exhibit a capacity of over 2000 $\mathrm{mAh/g}$. Additionally, the graphene coating assists the electron migration during the discharge/charge processes, which lead to an around 100% coulombic efficiency with no fading at various C-rates and a diminished irreversible capacity at the first cycle.

More recently, Zhao and Zhang et al. [57] described a beyond theoretical capacity $LiFePO_4$ cathode. The material presented was a composite of glucose-derived carbon-encapsulated LFP with internal carbon sheets synthesized by a hydrothermal-alcohol washing-calcination procedure employing phythic acid (PHyA) as a special phosphorus source and as internal carbon precursor. The as-prepared composite showed ultra-high specific capacity of $192\mathrm{mAh/g}$ at 0.1 C, and a remarkable rate of performance of $140\mathrm{mAh/g}$ at 10 C. The proposed explanation for the above-theoretical capacity was related to the reversible redox reaction between the Li^+ ions of the electrolyte and the oxygen groups at the defects in the internal carbon sheets. Meaning that the oxygenic groups effectively acted as interfacial storage sites. To further explain the increased ionic conductivity, three main reasons were presented. Firstly, the interplanar spacing of the bulk crystals of the internal carbon

sheets and the LFP core is larger than for standard LFP due to corner and edges, thus, facilitating lithium-ion diffusion. Secondly, the presence of internal carbons, which separated from PhyA and improve transportation of lithium ions and, finally, the overall unique structure of the composite. It is of note that the presented explanation for the beyond theoretical capacity is similar to the one presented before by Hu et al., potentially pointing to a pathway for ultra-high capacity LFP cathodes.

Although carbon coating, in its varied manifestations, is a very effective method of improving the electrochemical characteristics of LFP cathodes, by itself, pure carbon coating it is somewhat limited in its capabilities to obtain excellent performance [58]. Thusly, several modifications to carbon-coated layers have been proposed to optimize the carbon-coating process. Some of the modifications studied broadly include the use of nitrogen, phosphorus, boron, fluorine and sulphur for doping the carbon-coated layer [59].

Due to its high electronegativity compared to alternative doping elements such as boron and nitrogen, fluorine has great potential for modifying carbon-coated LFP cathodes by doping. This element forms covalent bonds with carbon, which are beneficial for electrolyte permeation, thus, improving electrochemical performance. In a recent work, exploring fluorine use for doping, Wang et al. [60] produced a fluorine-doped carbon coated LFP compound via a ball-milling assisted rheological phase method combined with solid state reaction, with polyvinylidene fluoride (PVDF) as a carbon and fluoride source. The unique structure of the fluorine-carbon coating and the presence of defects in such coating potentially provided redox-active sites for reversible lithium storage, consequently enhancing the rate capacity of the compound, were proposed as the explanation for the outstanding electrochemical properties observed. Concretely, a higher-than-theoretical value discharge capacity at $0.1\ \mathrm{C}$ of $174.3\mathrm{mAh/g}$ was obtained, alongside a high capacity of $100.2\mathrm{mAh/g}$ at $20\ \mathrm{C}$ and a good cycling ability after 1000 cycles.

Feng and Wang [59] were the first to dope carbon-coated LFP with boron, in an effort to improve performance electrochemical performance and the obtained composite, $LiFePO_4@B_{0.4}-C$, demonstrated a high reversible specific capacity of $164.1\mathrm{mAh/g}$ at $0.1\ \mathrm{C}$ and other remarkable properties such as enhanced carbon conductivity, due to increase in the number of hole-type charge carriers and improved Li storage capacity.

Nitrogen is an attractive alternative for doping of carbon-coated LFP. Due to the hydrophilic properties of nitrogen, the nitrogen-doped carbon (NC) layer impedes LFP aggregation and allows for a better dispersion of carbon materials across its surface. Additionally, nitrogen-doped carbon coating has been shown to improve electrochemical performance, namely cycle stability, rate performance and enhanced surface conductivity. The improvement in surface conductivity is due to the increase of electron carriers for conduction provided by the NC layer and the induced defects introduced in the structure, who increase Li^+ ions diffusion, which also lowers the energy barrier for lithium-ion diffusion kinematics [61, 62]. As a recent example of carbon-surface doping with nitrogen taking advantage of the properties discussed above, Xiong et al. [62] reported the controlled synthesis of nitrogen-doped carbon coated $LiFePO_4$ nanospheres via a facile hydrothermal method with a posterior chemical polymerization process. This composite demonstrated a high specific capacity of $158.4\mathrm{mAh/g}$ at $1\ \mathrm{C}$ after 200 cycles and a good rate capability of $107.5\mathrm{mAh/g}$ at $30\ \mathrm{C}$.

Doping carbon-coated LFP need not be restricted to a single element, indeed, some research as been conducted in leveraging properties of multiple elements to improve electrochemical performance of carbon-coated LFP. As an example of just that, Zhang et al. [63] produced a codoped carbon coated $LiFePO_4$ composite. The composite was synthesized by processing hydrothermally prepared carbon-coated $LiFePO_4$. This processing involved a ball-milling procedure followed by calcination at $600^{\circ}\ \mathrm{C}$. The doping of the carbon layer was conducted one element at a time, and it was found that the order in each element was introduced affected the performance. The addition of boron first, followed by nitrogen let to the formation of undesirable, non-conducting N – B configuration, which lowered electronic conductivity, which resulted in poor electrochemical performance. Conversely, it was found that introducing the elements in the opposite order eliminates the non-conducting configuration, while promoting the C – N configuration which markedly improved electronic conductivity and performance. This last codoping strategy led to synergistic electrochemical activity when compared to single doping of either element. The optimal codoped carbon-coated LFP composite displayed a high discharge capacity at $20\ \mathrm{C}$ of $121.6\mathrm{mAh/g}$, a large improvement over the pure carbon-coated LFP sample which only had a capacity of $101.1\mathrm{mAh/g}$ at the same rate.

There exist other types of modifications that can be performed on carbon-coated LFP to improve performance besides doping. For instance, co-coating LFP with metal oxides and/or ionic conductors, with the aim of improving electron conduction, Li transport and

optimizing charge balance[31, 64]. One work employing such modification was published by Shu et al. [65] where it was first reported the synthesis of a spherical LFP hybrid, coated with fast Li^+ conductive $La_{0.56}Li_{0.33}Ti_3$ perovskite oxide and electron-conductive carbon composite by an ammonia assisted hydrothermal method. The composite demonstrated excellent electrochemical performance even at high rates, with a discharge capacity of $62.3 \mathrm{mAh/g}$ at $30\ \mathrm{C}$. This performance was attributed to the unique morphology of the hybrid coating layer, which prevented erosion of the LFP electrolyte by HF and allowed for fast Li^+ and electron transport.

Although many more works exist covering different variations on these surface modification methods, they won't be covered in the present monograph due to time and space constraints.

3.1.3 Element Doping

Doping of LFP in the context of the surface modification of a carbon coating was explored extensively in the previous section. However, doping can be applied directly for LFP cathode optimization. Indeed, doping is one of the major strategies to improve electrochemical characteristics. Doping consists of replacing a small amount of lithium, iron and oxygen sites with other ions. This substitution allows for the enhancement of a variety of desirable properties, such as Li-ion diffusion, electronic conductivity and charge/discharge performance at high current densities. Doping can be single element, where Li^+, Fe^{2+} and O^{2-} are substituted with only one type of replacement ion or multielement, where multiple different kinds of ions are used. Multielement doping has attracted more attention in recent times and may allow for better electrochemical performance than its single-element counterpart.

The literature on this topic is vast, so a comprehensive coverage of all possible doping elements in all three of its possible sites within LFP is not within the scope of this work. Therefore, only a small selection of illustrative research will be discussed per dopable site alongside relevant context to understand the differences between the three possible doping targets.

Lithium sites in the $LiFePO_4$ structure can be replaced with a variety of other elements, generally, these elements have a smaller ionic radius, such as Al, V, K, Na, Nd and Zr. Utilizing these smaller ions improves electrochemical properties by decreasing the charge transfer resistance, while simultaneously increasing the width of the one-dimensional Li^+

diffusion channels. This improvement can manifest in an increase to electric conductivity, as Chung and Chiang [66] reported in their early work with LFP doped with Niobium. The extent of the increase when compared with undoped samples was massive, of around 6 orders of magnitude at room temperature. In recent works, Niobium doping was shown to also markedly enhance the reversible capacity, as demonstrated by Johnson et al. [67], who produced 1% doped LFP samples that achieved capacities of $156\mathrm{mAh/g}$ at 0.5 C and $110\mathrm{mAh/g}$ at 10 C.

It has also been reported that doping in lithium sites can Li create vacancies, which improve capacity. Chiang et al. [68] demonstrated just that in their work with Vanadium doping of nano-sized LFP cathodes into the lithium sites. The doped cathode demonstrated superior electrochemical properties compared to the pristine LFP sample. The capacity improved from $138\mathrm{mAh/g}$ to $155\mathrm{mAh/g}$ at 0.1C and the conductivity increased by a factor of 40, from $4.75x10^{-4}$ S/cm to $1.9x10^{-2}$ S/cm. In their landmark work, Chung et al. [66] studied, among other things, the use of aliovalent cations, such as Mg^{2+} and Mg^{3+}, in lithium site doping, proposing that the introduction of these ions allowed for the generation of Li^{+} ions and for the stabilization of solid solutions with a net cation deficiency. The work of Wagemaker et al. [69] proposes that the additional charge of the aliovalent dopant is often balanced by lithium-ion vacancies generation, thus, not being responsible by an improvement in conductivity. Additionally, the introduction of immobile high valency dopants may hinder Li^{+} diffusion.

Iron-site doping in $LiFePO_4$ facilitates Li^{+} diffusion, which leads to enhanced speed in lithium storage, improvements in ionic and electronic conductivity and discharge capacity of LFP cathodes. This is widely attributed to the role the doping agent plays in both limiting crystallite growth and size and in facilitating formation of active sites for nuclei [70, 71]. Due to this, iron-site doping is the most widely studied for use in LFP.

Using magnesium as the doping element, Örnek and Efe [72] reported the synthesis by sol-gel-assisted CTR of carbon-coated $LiFe_{0.96}Mg_{0.04}PO_4$ and obtained good electrochemical performance, with the discharge capacities measured to be high at varying discharge rates. More concretely, $167\mathrm{mAh/g}$ at 0.1C, $155\mathrm{mAh/g}$ at 0.2C, $141\mathrm{mAh/g}$ at 2C, $103\mathrm{mAh/g}$ at 10C, $92\mathrm{mAh/g}$ at 20C, with 97% of the discharge capacity remaining after 300 cycles.

Vanadium is a widely used ion for doping of LFP. It has been shown that by the alteration of the structure of $LiFePO_4$, generation of vacancies and possessing various oxidation

states, alongside the formation of active phases, such as $LiVOPO_4$, and avoidance of impurity phases, vanadium doping decidedly improves Li^+ diffusion and electrochemical performance, principally at high current rates [73]. In a recent work, Jiang and Wang [74] produced vanadium doped carbon-coated $LiFe_{1-x}V_xPO_4$ by a sol-gel method, and studied its electrochemical properties. The composite improved both the discharge and reversible capacity when compared with undoped carbon-coated LFP, with values of $162.9\mathrm{mAh/g}$ at $0.1\mathrm{C}$ and $112\mathrm{mAh/g}$ at $10\mathrm{C}$ (after 200 cycles), respectively. The discharge capacity obtained is around 95.8% of the theoretical value.

A promising and comparatively understudied element for LFP doping is nickel. One advantage that has been reported over other elements is the stabilizing nature of Ni^{2+} on the LFP structure, as Örnek et al. [75] demonstrated in their study of Nickel-doped, carbon-coated $LiNixFe_{1-x}PO_4$ cathode material. The synthesis was done using a sol-gel assisted carbothermal reduction technique and the sample demonstrated a high discharge capacity at $155\mathrm{mAh/g}$ at $0.2\mathrm{C}$, a stable cycle life and null capacity fade. These results were attributed to the more stable lattice structure and improved Li^+ diffusion due to Ni^{2+} serving as pillars in the crystalline structure, preventing its collapse during cycling, alongside the expected enhanced electrical conductivity.

In a relatively recent work, Zhang et al.[76] calculated the impact of several doping elements in the electrochemical properties of doped LFP from first principles. The elements covered were Co, Mo, Mn and Nb and it was demonstrated that the dopands can improve mechanical stability and reduce aninsotrpy, which reduces the risk of shear deformation and microcracking in the material, which can cause polarization of the electrode and, consequently, fade in capacity. The effects of copper on shear resistance were of particular note. Additionally, it was shown that these elements reduce the bang gap of LFP, in particular Co and Nv, which facilitates the electronic transition.

Oxygen-site doping was predicted, from first principle calculations, to improve conductivity even more than their iron-site counterpart. This is because, unlike with cation doping, O-site doping expands the *a* and *b* lattice parameters, while not affecting *c*, which causes a suppressing of antisite defects in LFP. This was later shown experimentally, for instance, in the work of Okada et al. [77] in which sulphur doped LFP nanoparticles, synthesized via solvothermal method with thioacetamide used as a sulphur source were studied. The nanoparticles showed an improved reversible capacity when compared to undoped samples, with a high value of $113\mathrm{mAh/g}$ at $10\mathrm{C}$ being reported. These results

were, as predicted theoretically, attributed to lattice expansion and the suppression of Fe – Li antisite defects by the anion-dopant, which expanded the diffusion pathways and allowed for Li^+ ions movement without blockage.

Several authors have reported the use of fluorine for doping LFP with the aim of improving electrochemical performance [78, 79]. In a recent work, Li et al. [79] synthesized a carbon-coated LFP composite doped with fluorine. The synthesis of the F-doped $LiFePO_{4-x/3}F_x$/C was done via a wet mechanical agitation-assisted high-temperature ball milling method and the amount F-doping done was varied. It was found out that the optimal results were obtained for $x = 0.06$, with the sample demonstrating high initial discharge capacities of $162.6\mathrm{mAh/g}$ at $0.1\mathrm{C}$, $156.6\mathrm{mAh/g}$ at $0.5\mathrm{C}$, $150.2\mathrm{mAh/g}$ at $1\mathrm{C}$, $144.5\mathrm{mAh/g}$ at $2\mathrm{C}$, $131.6\mathrm{mAh/g}$ at $5\mathrm{C}$ and $115.8\mathrm{mAh/g}$ at $10\mathrm{C}$. Moreover, the discharge capacity at $10\mathrm{C}$ after 100 cycles was $110.5\mathrm{mAh/g}$ which translates to a 95.4% retention rate. The reason provided for the improvement in electrochemical performance was the improved Li-ion diffusion, enhanced structural stability and electronic conductivity.

Moving on to briefly discussing multielement doping (also known as co-doping), this type of modification to LFP, as stated before, has gained notoriety due to its possible improvement over its single-element counterpart. It can be performed in two distinct ways, one can dope with different elements in different sites or with different elements in the same LFP sites.

As an example of co-doping in the same site, in particular the Fe-site, one can look at the work of Tu et al. [80] who studied magnesium-titanium co-doping. In it, porous Mg-Ti co-doped $LiFe_{0.985}Mg_{0.005}Ti_{0.01}PO_4$ was synthesized via carbothermic reduction reaction combined with a spray drying process, with $FePO_4$ as a phosphorous and iron source. When compared to undoped samples, the co-doped microspheres demonstrate a great improvement, both in high-rate discharge capacity and other electrochemical properties, such as electronic conductivity and Li^+ ion diffusion coefficient. More explicitly, the discharge capacity at $0.2\ \mathrm{C}$, $0.5\ \mathrm{C}$, $1\ \mathrm{C}$, $3\ \mathrm{C}$, $5\ \mathrm{C}$ and $8\ \mathrm{C}$ were $161.5\ \mathrm{mAh/g}$, $160.6\ \mathrm{mAh/g}$, $156.7\mathrm{mAh/g}$, $147.5\mathrm{mAh/g}$, $139.8\ \mathrm{mAh/g}$ and $131.5\mathrm{mAh/g}$. respectively, with capacity retentions above 92% for the rates of $0.5\ \mathrm{C}$, $1\mathrm{C}$ and $5\ \mathrm{C}$. As for conductivity and diffusion coefficients (charge/discharge), the values measured were $1.58x10^{-3}\ \mathrm{S/cm}$, $5.97x10^{-9}\ \mathrm{cm/s}$ and $4.30x10^{-9}\ \mathrm{cm/s}$.

As for co-doping of different elements in different sites, Tian et al. [81] investigation on the synergistic effects of niobium and titanium as co-doping agents on both lithium and iron

sites in graphene-coated LFP is illustrative. Using a sol-gel method, followed by a mixing of graphene oxide with precursor and ball milling at room temperature, a graphene-coated $Li_{0.99}Nb_{0.01}Fe_{0.97}Ti_{0.03}PO_4$ composite was obtained. It was found that the electrochemical properties of the composite were excellent, with a high discharge capacity of $161.5 \mathrm{mAh/g}$ at $0.1\mathrm{C}$ and outstanding capacity retention of 99.1% after 30 cycles. These results were attributed to electron compensation caused by Ti^{4+} and Nb^{5+} ions in the structure, alongside the three-dimensional conductive network of graphene, the electrochemical properties.

3.2. Recent developments in Simulation of LFP cathodes

As stated previously, a great deal of the literature employing numerical simulations of Li-ion batteris involves thermal management and heat flow. As an example, Kong et al. [82] used the OpenFOAM framework to develop a three-dimensional thermal runaway (TR) model coupled with five exothermic decomposition reactions and internal short circuit to study the effects of heat generation, heat loss and external heat in the TR behaviours of two materials, $LiFePO_4$ and $Li_4T_{15}O_{12}$ (LTO). Notably, it concluded that batteries using LFP cathodes showed the best thermal safety and stability compared to other cathode materials, which is relevant, as thermal runaway is one of the main obstacles to expanding use of LIBs for more applications, as it can result in explosion or fire accidents. Henriksen et al.[83] also used the OpenFOAM platform to develop a method for CFD simulation of a premixed explosion of gas vented during Li-ion battery failure. Maximum explosion pressure and flame front position were simulated and agreed well with experimentally obtained results. The accuracy of the temporal evolution of the simulation, however, was limited. Simulations methods have also been used to study the impact of tab design in large-format Li-ion cells. Zhao et al. [84] conducted such research, by developing a three-dimensional methodology based on electrochemical and physical principles underpinning the functioning of Li-ion cells. In their work, by maximizing the use of active material and minimizing voltage loses, it was demonstrated a noticeable increase in the usable energy of large cells. In particular, they proposed a class of designs utilizing multiple current-collecting tabs, which minimize in-plane electron transport losses and achieve energy density on par with regular-sized cells.

Moving to a work with LFP batteries, Nazari et al. [85] used the Newman's P2D model, alongside White's heat generation model to study the energy efficiency of a LFP/Graphite cell at a variety of different temperatures, ranging from 283.15 K to 313.15 K . The model was validated utilizing a commercial LFP/Graphite LIB, with thorough characterization

of the heat generating sources in the cell. The total heat generation of the battery was calculated and charge/discharge efficiency plots at different temperatures were obtained which agreed very well with the experimental data. In subsequent work [86], Nazari et al. proceeded with the simulation work, studying the low temperature efficiency, not only of an LFP battery, but also Lithium manganese oxide (LMO) and Lithium cobalt oxide (LCO) batteries. Using the same pair of simulation models as in their previous paper, the battery efficiency plots for each battery at different operation conditions were obtained and, again, well with the experimental data. Both of these works aid in the development of new batteries by allowing for accurate predicition of their efficiencies at low temperatures.

4. Methodology

Initially, it was planned to use the battery simulation software developed by Yang et al.[87] based on the open-source OpenFOAM project to conduct the work required. However, significant technical difficulties required a change of software.

The *Ansys Workbench* platform was chosen to develop all the work due to its ease of use, availability and extensive know-how from colleagues. Thus, all the work in the simulation process, from the design of the geometry, to meshing to the simulation itself was done using it.

The subsequent sections go over the different steps of the work conducted, detailing each part of the simulation process that was done, starting with a thorough explanation of the *Ansys* software and its implementation of the P2D model. Without this initial discussion, it would be impractical to describe the work conducted in an understandable way. To use the P2D model in *Ansys Fluent*, the Battery Model module is activated within the software and then chosen from a list of options.

4.1. Newman P2D Model within *Ansys Fluent*

4.1.1 Mathematical Implementation

Ansys Fluent implements the Newman P2D model using a Multi-Scale Multi-Domain approach (MSMD) [88]. This is required due to the different length scales present within the physics of Li-ion battery modelling. Indeed, the physics governing the Li^+ ion transport in the active material itself occurs in the atomic length scale, while the flow of the Li^+ ion across the anode, through the separator into the cathode occurs in the scale of the electrode itself. The MSMD approach allows for solving these different physical processes in different solution domains.

The structure and anatomy of the battery within *Ansys Fluent* implementation of the PD2 model is identical to the one described in chapter 2. However, the governing equations were rewritten, combined and simplified for use of the MSMD approach and for the sake of computational efficiency [88]. The details of the rewriting employed are beyond the scope of this work. The rewritten equations are now presented.

The Lithium conservation in the solid phase and the electrolyte phase are described by equations 4.1 and 4.2 respectively:

$$\frac{\partial c_s}{\partial t} = \frac{D_s}{r^2}\frac{\partial}{\partial r}\left[r^2\frac{\partial c_s}{\partial r}\right] \tag{4.1}$$

$$\frac{\partial\left(\varepsilon_e c_e\right)}{\partial t} = \frac{\partial}{\partial x}\left[D_e^{eff}\frac{\partial c_e}{\partial x}\right] + \frac{1-t_+^0}{F}j^{Li} \tag{4.2}$$

It's important to note that equation 4.1 is solved in the electrode zone across every discretized spacial location, meaning, at every individual spherical particle. This integration across the radius of each particle is a pseudo second dimension, which explains the P2D designation in literature.

The charge conservation in the solid phase and the electrolyte phase are described by equations 4.3 and 4.4 respectively:

$$\frac{\partial}{\partial x}\left[\sigma^{eff}\frac{\partial \varphi_s}{\partial x}\right] - j^{Li} = 0 \tag{4.3}$$

$$\frac{\partial}{\partial x}\left[k^{eff}\frac{\partial \varphi_e}{\partial x}\right] + \frac{\partial}{\partial x}\left[k_D^{eff}\frac{\partial \ln c_e}{\partial x}\right] + j^{Li} = 0 \tag{4.4}$$

The Butler-Volmer equation is written as:

$$j^{Li} = a_s i_0\left\{\exp\left\{\frac{\alpha_a F}{RT}\eta\right\} - \exp\left\{-\frac{\alpha_c F}{RT}\eta\right\}\right\} \tag{4.5}$$

Where the overpotential η is defined by:

$$\eta = \varphi_s - \varphi_e - U \tag{4.6}$$

And the exchange current density, i_0, is defined by:

$$i_0 = k_m(c_e)^{\alpha_a}(C_{s,max} - c_{s,e})^{\alpha_a}(c_{s,e})^{\alpha_c} \tag{4.7}$$

The electrolyte ionic diffusivity, conductivity, diffusional conductivity and the solid phase electric conductivity are also defined by a group of seven equations and can be consulted in the Ansys Theory Guide [88]. They were not presented here due to their limited interest

for the understanding of the functioning of the model.

Additionally, *Ansys Fluent* also solves for the thermal and electric fields at the battery cell's scale,*, using the following differential equations:

$$\frac{\partial \rho C_p T}{\partial t} - \nabla \cdot (k \nabla T) = \sigma_+ \left|\nabla \phi_+\right|^2 + \sigma_- \left|\nabla \phi_-\right|^2 + \dot{q}_{ECh} + \dot{q}_{short} + \dot{q}_{abuse} \tag{4.8}$$

$$\begin{aligned} \nabla \cdot \left(\sigma_+ \nabla \varphi_+\right) &= -\left(j_{ECh} - j_{short}\right) \\ \nabla \cdot \left(\sigma_- \nabla \varphi_-\right) &= j_{ECh} - j_{short} \end{aligned} \tag{4.9}$$

With their source terms being computed as:

$$j_{ECh} = -\frac{Q_{nominal}}{Q_{ref} Vol} i_P \tag{4.10}$$

$$\dot{q}_{ECh} = \frac{i_P V + \int_{l_p+l_s+l_n}^{0} j^{Li} \left(T_{ref} \frac{\partial U}{\partial T} - U_{Ref}\right) dx}{l_p + l_s + l_n} \tag{4.11}$$

Respectively.

And where l_p, l_s and l_n correspond to the thickness of the positive electrode, the separator and the negative electrode respectively, and i_p is the transverse current density:

$$i_P = \int_0^{l_p} j^{Li} dx \tag{4.12}$$

Equation 4.10 is also used to go from the scale of the battery cell to the electrode scale regarding the current transfer rate, in this way connecting the two.

4.1.2 Model Parameters

As discussed in chapter 2, Newman's P2D model requires a large number of parameters. Its implementation within *Ansys Fluent* is no different. First, it's important to discuss the material database, which bundles several parameters related to the cathode, anode and separator materials. These parameters are necessary for solving the model solution, however, some cannot be directly changed in the interface.

*This is an addition to the original P2D model

For the cathode and anode these parameters are: Rate constant, Anodic transfer coefficient, Cathodic transfer coefficient, Bruggman Tortuosity Exponent, OCP (Open Circuit Potential), Diffusivity (in m^2/s) and Diffusivity (in S/m). OCP, Diffusivity and Conductivity can be given as either as a constant, a piecewise-linear function or a polynomial function. While for the electrolyte we have: Bruggman Tortuosity Exponent, Diffusivity, Ionic Conductivity, t+ Factor and the Activity term.

Another important concept that is mentioned below is State of Charge (SOC). SOC refers to the amount of charge that is present in the battery at any given point during the charge or discharge process. For a full discharge, ideally, a cell would go from an SOC of 1 (or 100 %) to 0 (or 0 %), and the inverse for a charging process.

Now, we will enumerate the different parameters and, when applicable, how they relate to the equations discussed before [89]:

- **Number of Grids** and **Number of Grids in solid** - The first must be defined for all three regions, positive and negative electrode and separator, and the latter only within the positive and negative electrode. This make sense, as the electrolyte phase in the P2D model is transversal across the battery, while the solid phase only exists within the electrodes. These parameters correspond to the number of grid points that will be used to discretize the electrolyte phase and the spheres of particles which constitute the solid phase.
- **Grid Size Ratio** and **Grid Size Ratio in solid** - Parameters that also affects the underlying mesh, allowing for the creation of bias within the electrolyte or solid phase respectively, in one electrode over the other, for geometries that might require such treatment.
- **Thickness** - Refers to the thickness of each region, the two electrodes and the separator. They appear explicitly in equation 4.11.
- **Particle Diameter** - Refers to the particle diameter in the active material.
- **Cs,max** - Refers to the maximum concentration of Lithium in the solid phase. Used in equation 4.7.
- **Stoi. at 0% SOC** and **Stoi. at 100% SOC** - Refer to the stoichiometry at 0% and 100% respectively. Both are used to calculate the initial lithium concentration in the electrodes and the theoretical capacity.

- **Init. Cs** and **Init. Ce** - Refers to the initial concentration in the electrodes. Cannot be specified by the user but rather is calculated internally by the software.
- **VOF of Electrolyte** and **Filler fraction** - Refer to the volume fraction of the electrolyte material in the electrode and the volume fraction of the filler material in the electrode, respectively. In other words, describes which fraction of each battery component's volume is active material, filler and electrolyte. The values of all three must sum to 1. Note that the volume fraction of active material is defined implicitly.
- **Ds** - Refers to the diffusion coefficient of Li^+ in the electrodes at the reference temperature of 25 C.
- **Activation Energy** E_r - Refers to the activation energy that controls the temperature sensitive of the reaction constant used as a reference.
- **Trans. Coef. a** and **Trans. Coef. c** - Refer to the charge transfer coefficient at the anode and the cathode, respectively. Used in equation 4.7 as α_a and α_c respectively.
- **OCP** - Refers to the open circuit potential of the electrode materials. It's usually a function of the state of lithiation (SOL), which is calculated as $\frac{c_s}{c_{s,max}}$. It can be defined as a User Defined Function (UDF) or as piece-wise linear function. Used in equation
- **De** - Refers to the diffusion coefficient of the lithium inos in the electrolyte phase.
- **t+ Factor** - Refers to the transference number of lithium ions.
- **Ionic Cond** - Refers to the ionic conductivity of the electrolyte.
- **Activity term** - Refers to the activity related term $\frac{d \ln f_{\pm}}{d \ln c_e}$ present the equation that describes the electrolyte diffusional conductivity *.

An image of the graphical interface can be seen in 4.1.

4.1.3 Additional software setting with impact on the model

Ansys Fluent contains some additional settings that while not directly connected to the P2D model affect the simulation results. These settings will be discussed below.

*This equation wasn't presented above, but it was mentioned

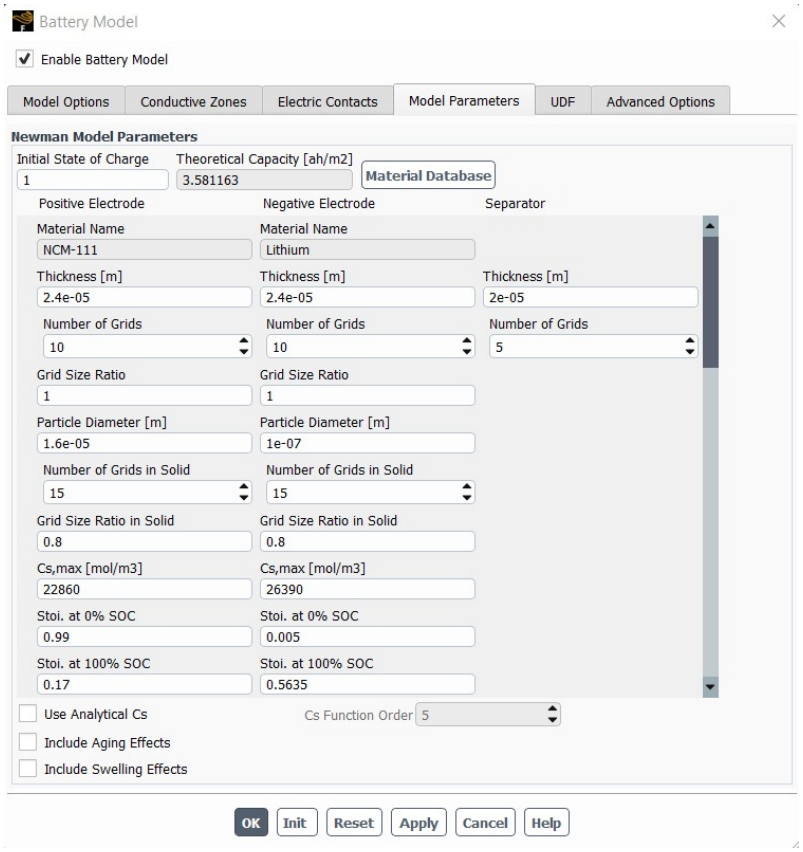

Figure 4.1: Graphical interface of the Parameter tab of the Battery Model window in *Ansys Fluent*

4.1.3.1 Fluent Materials

Fluent's Material tab allows the addition of different materials to give specific properties to different section of the geometry used. These materials can be fluid or solid, and added directly or imported from several material databases.

The values available to describe the material vary depending on the Models which are used. When activating the Battery model, the available ones are: Density ($\mathrm{Kg/m^3}$), CP / Specific Heat ($\mathrm{J/(KgK)}$, Thermal Conductivity ($\mathrm{W/(mK)}$ and Electrical Conductivity ($\mathrm{S/m}$). These values can be constant or defined as functions by the user.

In the case of the P2D model, there is overlap in parameters for the electrodes in the *Fluent*'s Material tab and the model interface, which causes the values defined in the model interface to take precedent. Due to this, the only defined materials were for positive and negative current collectors, these being copper and aluminium respectively.

4.1.3.2 Cell Zone and Boundary conditions

The Cell zone conditions tab allows choosing the material of the different zones previously defined in the geometry. Zones can be either fluid or solid. All the zones for this work are treated as solids. It also allows altering conditions of the geometry, such as its frame of reference and orientation, solid motion, mesh motion, among others. However, these are not relevant for battery simulation as the battery is taken to be static.

The boundary condition tab is divided into two different types of boundaries for the geometry used: Internal and Wall. Walls represent the external barriers of the geometry and are connected to the mesh cells only on one side, while internal interfaces act as the boundaries of different regions of the geometry and are connected to the cells on both sides [89].

Walls can be configured to have many different properties, if specific modules are activated, however, in this work, only the battery model is used. Given this, the only configuration required is related to the thermal conditions. The thermal mode chosen for the walls was convection, with a fixed initial temperature and a heat transfer coefficient of 5 $\mathrm{W/m^2K}$, as recommended in the *Ansys User Guide* [89].

4.2. Step by Step of the Simulation process

In this section, the work conducted is explained step by step, with each different part of the process expanded upon.

4.2.1 Geometry

To simulate with *Ansys Fluent*, it is necessary to construct a suitable geometry. The *Ansys* suite of products allows for several different programs for this purpose, while also allowing importing pre-made geometries from other sources. In this work, *DesignModeler* was chosen to build the geometry due to its relative simplicity and ease of use. To fix issues with surface sharing and duplication, *SpaceClaim* was used.

The geometry used in this work was of a simple coin-cell, composed of 3 concentric cylinders layered on top of each other. The top and bottom layer representing the positive and negative current collectors, respectively, and the middle one the electrolyte. Several were made with different thicknesses as needed. An illustrative diagram can be seen on fig 4.2.

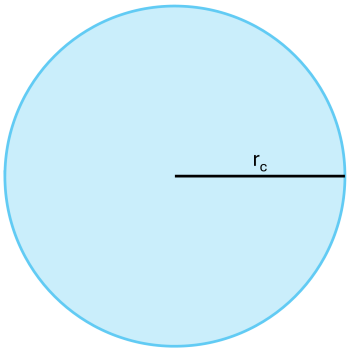

(a) Top view

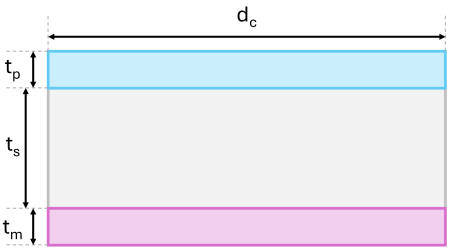

(b) Side View

Figure 4.2: Diagrams representing the geometry used.

4.2.2 Meshing

Meshing consists of dividing a given geometry into small, discrete elements (or cells) that serve as the domain where the partial differential equations will be solved in each simulation step. There are different types of meshes. For 3D geometries, *Ansys Fluent* allows for meshes composed of tetrahedral, hexahedral, polyhedral, pyramid or wedge cells or a mixture of several types. Tetrahedral and triangular meshes are recommended for more complex geometries, with hexahedral/quadrilateral meshes recommended for simple ones.

Given the simplicity of the geometry used in this work, a hexahedral/quadrilateral mesh was used, to avoid unnecessary computational work.

As mentioned earlier, the software used for meshing is part of the *Ansys Workbench* platform and integrated with *Ansys Fluent*, allowing for a smooth transition between creating the mesh and simulation.

4.2.2.1 Mesh parameters and Validation

The most common parameters used to evaluate the quality of a mesh are element size, skewness, element quality, aspect ratio and orthogonal quality. The goal with the meshing process is to obtain the highest quality mesh possible within existing constraints.

Element size is chosen a priori and is constrained by two key factors, meshing time and software limitations. For an element size under 1×10^{-4} m, the meshing time increases exponentially and when it reaches 1×10^{-5}m the software fails to mesh due to a memory issue. Some tests were made with different thicknesses and, while the specific value for the elements size varied slightly, it was always around the 10^{-5} m value, with 1 million elements in the mesh appearing to be a hard limit for the software with the settings used.

Skewness is defined as the normalized difference between the distance from the line connecting two adjacent cell centroids and the shared face's centre. More simply, it's the difference between the shape of a given cell when compared to an equilateral cell of equivalent volume. The value can range from 0, which is ideal, and infinity. As a general rule, to obtain a good mesh, the average skewness should be around 0.33 with the maximum skewness below 0.90. At higher maximum values, convergence issues may arise and lead to bad results [89]. Taking this into consideration, in this work, we aimed to keep all meshes generated within these range of values for skewness.

Element quality measures how different from a perfect cube or tetrahedron a given element is, and is defined as the volume divided by the sum of the square of the edge lengths. A good value for the average element quality is above 0.3. In tetrahedral meshes.

The aspect ratio measures the stretching of the cell. It is calculated as the ratio of the maximum value between the normal distances of the cell centroid and the nodes or the normal distance between the cell centroid and the face centroids. This computation is done as the dot product of the distance vector and the face normal. For a unit cube, the aspect ratio is 1.732. The closer a given cell is to this number, the more it approximates a cubic cell. A charge change in aspect ratios across the mesh is undesirable and should be avoided.

Orthogonal quality, within *Ansys Fluent*, is calculated from a quantity known as orthogonality. For hexahedral and polyhedral cells, like the ones used in this project, the orthogonality is simply equal to the orthogonal quality. However, for pyramid, prism and tetrahedral cells, the orthogonal qualities is the minimum of the orthogonality and 1 cell skewness. The orthogonality of a given cell is defined as the minimum value between two different calculations: the normalized dot product of the area vector of a face ($\vec{A}_i$) with the vector from the centroid of the cell to the centroid of that face ($\vec{f}_i$).

$$\frac{\vec{A}_i \cdot \vec{f}_i}{|\vec{A}_i||\vec{f}_i|} \tag{4.13}$$

And the normalized dot product of the area vector of a face ($\vec{A}_i$) and the vector from the centroid of that same cell to the centroid of an adjacent cell that shares that face ($\vec{c}_i$).

$$\frac{\vec{A}_i \cdot \vec{c}_i}{|\vec{A}_i||\vec{c}_i|} \tag{4.14}$$

Following from these equations, the cells with low orthogonality, and therefore low orthogonal quality, will have values closer to 0, while the highest orthogonality, and therefore high orthogonal quality, will have values close to 1. To obtain good results, the minimum value for orthogonal quality should be 0.01 with an average value significantly above that.

To ensure the quality of the mesh for the desired simulation work, a validation process was conducted. This process consisted of varying the element size and using a simulation result whose expected value is known to analyse how the variation of element size affects the value, if at all, and weight that variation with the computational resources and time used. Additionally, the mesh quality parameters are compared and their proximity to the recommended values is also noted. In this work, the cell capacity was used as the mesh validation parameter.

In *Ansys Fluent*, the default values for a NMC cell with a graphite anode were used, and several simulations were made for different element sizes, and the value for the capacity was registered. The choice of running the validation test with default values for an NMC cell was made mainly for time related reasons. Using the default values avoids the time-consuming process of finding adequate parameters and ensures that the simulation will run without issues caused by them. Additionally, the value itself is not important, just its variation and tendency relating to element size, as those factors should be transversal to

simulations using different materials and parameters.

Six different elements sizes were chosen for validation, ranging from a maximum size of 1 m to 0.00005 m. The maximum and average values obtained for each parameter discussed previously can be seen in table 4.3, alongside the approximate simulation time.

Element Size (m)	Nº Elements	Skewness		Element Quality		Aspect Ratio		Orthogonal Quality	
		Max	Average	Max	Average	Max	Average	Max	Average
1	30	0.50492	0.38362	0.30604	0.20166	15	11.4	0.96158	0.90169
0.1	111	0.41194	0.23606	0.43708	0.3724	6.9491	5.3722	0.99898	0.97045
0.01	111	0.41194	0.23606	0.43708	0.3724	6.9491	5.3722	0.99898	0.97045
0.001	477	0.67595	0.16032	0.95265	0.72908	3.3589	2.3905	0.99816	0.97135
0.0001	111276	0.5902	7.02E-02	0.99989	0.96353	5.1349	1.2641	0.99998	0.99037
0.00005	718977	0.66163	6.29E-02	0.99995	0.95978	7.3898	1.2677	1	0.99093

Figure 4.3: Mesh validation parameters for each element size.

As was expected, with the reduction of the element size, and consequent increase in the number of cells, the values for each measurement improve overall. However, for skewness we can see an increase in its maximum value and in element quality a decrease in the average value when decreasing the size from 0.0001m to 0.00005 m. This can be explained by noting that, with the increase in the number of cells by a factor of almost 7, more cells with a poorer quality in these parameters will be present, slightly increasing the average value in the element quality and the maximum value in the case of skewness, even when the overall quality of the mesh increases. Which is reflected in the fact that the minimum value for both parameters decreases. Regardless, the values for all parameters are well within the recommended range, even with a very coarse grid, and especially for the meshes with a high element size, for which the values are almost perfect. The time increases drastically, going from an element size of 0.0001 m to 0.00005 m due to the aforementioned increase in the number of cells. The parameter chosen for validation, cell capacity, shows a very similar result. Indeed, increasing the minimum element size above causes the simulation time to go from 2 to 8 hours depending on the number of time steps chosen, to well over 2 days of running time on an average machine.

Indeed, the value for cell capacity is equal for all the simulations ran, up to the ninth decimal place, which is far beyond experimental accuracy. This can be explained by the size and simplicity of the geometry. The coin-cell has no sharp corners or complex details, and thus, even with relatively big element sizes, the solution for the model's equation converge and result in the same capacity value.

Considering these results, the mesh element size chosen for this project was 100 μm. The mesh used for the simulation work conducted can be seen in figure 4.4

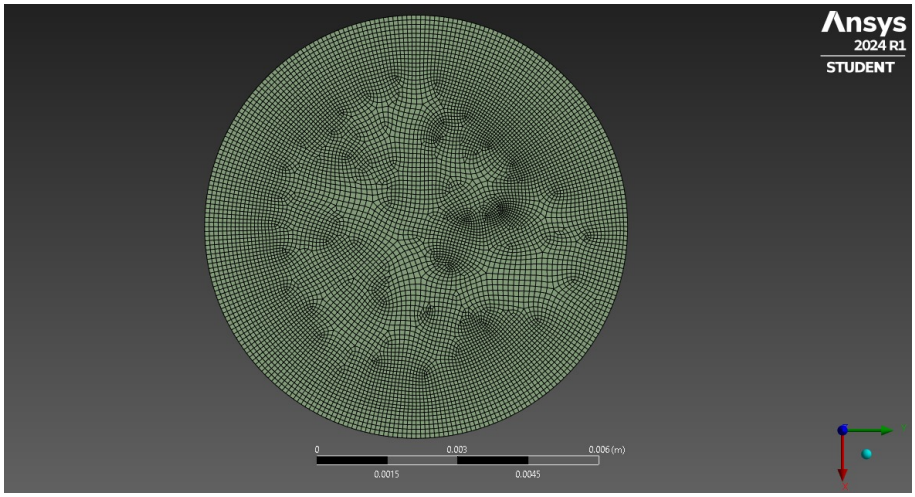

(a) Top view

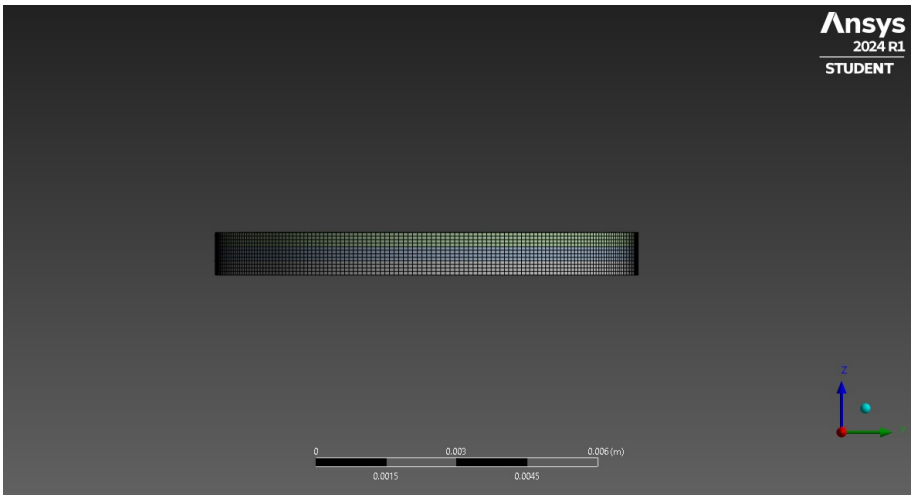

(b) Side View

Figure 4.4: Images of the mesh used from different perspectives.

4.2.3 Battery simulation with Ansys Fluent

The simulation work conducted consisted of three distinct phases: an adaptation period, model validation and a study of variation of parameters. In the adaptation period, different tests were conducted to get familiar with the user interface and the different parameters. These tests were important as they revealed crucial information regarding the software's functioning.

It was decided that five distinct measurements would be recorded within the simulation: **Battery temperature**, **Battery Current** at the terminal, **Battery Voltage** at the terminal, the **Flow Time** and the **State of Charge** (SOC).

Many more measurements could be recorded, such as the average concentration of the Li^+ ions or electrons across the different zones, however, doing so would increase the

duration of the simulation considerably and would add very little information related to the objectives of the work. Additionally, there were major technical issues in getting these measurements to begin with. Therefore, such data was not recorded. The measurements are registered at every time step, with each time step representing a given period of simulation time. In each time step, the software does several iterations until convergence, or until a maximum number is reached. The size of the time step is user defined, as is the number of time steps and the maximum number of iterations per time step. The higher the number of time steps and the lower their size, and the higher the number of iterations per time step allowed, the more accurate the simulation will be, however the computational cost increases exponentially.

Given that all the work was conducted for a C-rate of 1, 3600 times steps with a time step size of 1 would be ideal. However, this proved unfeasible due to the large amount of time required for each simulation. After some testing and consulting colleagues with more experience with simulation work, it was decided that the optimal values for these parameters for balancing simulation accuracy with time per simulation were 360 times steps, with a time step size of 10 and a maximum number of iterations per time step of 40.

The capacity of the battery would be calculated using the current values registered at each time step n, $current_n$, through the standard formula:

$$\text{Capacity} = \sum_{n=0}^{n=360} \frac{1}{3600} i_n \Delta \text{t} \tag{4.15}$$

Where Δt is the time step size.

All the graphical analysis was then conducted in Python, after reading the data generated by *Ansys Fluent*.

4.2.3.1 Model Validation - NMC battery

The model validation process consists of using an existing battery whose characteristics are known and ensure the model can accurately replicate them. For this work, a NMC half-cell was chosen.

Initially, the plan was to use an LFP half-cell, however, there was no reliable way of obtaining all the necessary parameters from a commercial one within the timeframe of this project. However, an NMC half-cell had been created by a colleague at CeNTI, Pedro Sampaio, for his dissertation work [90], which had all the necessary information related

to its structure easily available. Additionally, the charge/discharge cycle information had already been compiled, thus avoiding the time-consuming work of running such tests on a new battery.

Within the software, this change was easy to accommodate, as NMC comes as a default cathode material in the Material database, unlike LFP, which was added manually. As for the other parameters, some were taken directly from [90] or estimated from the existing cell, namely, cathode and anode thickness, particle diameter, the different stoichiometries and the volume fraction of electrolyte material, while others were chosen based on the literature and recommended settings from *Fluent* itself.

In theory, validating the model for one cathode material ensures that it is valid for other cathode materials.

The Validation process proved challenging.

To start, while the P2D model is capable of simulating half-cells, *Fluent*, does not come with that functionality already implemented. A half-cell consists of using lithium metal for one of the electrodes. If the negative electrode is replaced, it's called a cathodic half-cell, if the positive electrode is replaced, it's an anodic half-cell. Half-cells usually display a higher capacity when compared to the full-cells.

To allow for half-cell simulation, it was necessary to manually add metallic Lithium to the material database in *Fluent* and find the remaining parameters. These values were obtained from literature, and the individual source for each parameter can be consulted in Appendix 6.

A geometry was created to be as similar as possible to the half-cell created by [90], a mesh generated with the specifications described previously, and the parameters introduced into *Ansys Fluent*. Then the simulation was done and, afterwards, the results were analysed and compared to the experimental data.

4.2.3.2 Thickness variation analysis

After validating the model, a discussion with the supervisors and the other colleagues at CeNTI was had to decide which parameters were practical to vary and useful to study.

Many of the developments discussed in chapter 3 proved very hard or even impossible

to implement. For instance, different morphologies for the solid phase are not possible, given that, as previously mentioned, the model assumes uniform spherical particles. Other changes, such as treating the solid phase particles with a phase boundaries to more closely model real-life electrodes, while interesting and theoretically possible, would require an amount of time beyond the one allowed for this project and the technical know-how of the author to implement.

Another potentially interesting avenue of study was variation of particle size. However, this too proved not practical. The model is very sensitive to particle size. It was noted that without carefully tuning of particle size with electrode thickness, the simulation would fail early, and no useful results could be obtained. Given the objectives of this work, variation of a parameter such as this one would not be of use, as it could not be isolated from other simulation values.

With this being the case, a consensus was reached to study the effect of the variation of thickness of the electrodes, and its impact on the capacity and discharge behaviour of the LFP coin cell. The advantages of using the variation of thickness are threefold. First, thickness control can be controlled for during the fabrication process with relative ease, so being able to predict the effects that varying the size of the positive and negative electrode by specific amounts will have on the battery performance is very useful. Secondly, the expected behaviour is broadly known, therefore it is easy to verify if the simulation model fails or produces results not matching established electrochemical principles. And, from a practical standpoint, it's very easy to implement, due to the thickness of the different zones being able to be changed directly in the software interface.

It was decided that, to study the impact of electrode thickness on the coin cell performance, it would be varied in the following way:

- Thickness of the positive electrode equalling the thickness of negative electrode for 50, 100, 200 and 400 micrometers.
- Thickness of the positive electrode and negative electrode being 100 and 200 micrometers respectively, and the inverse.

These values for thickness were chosen to represent a broad range of measurements that are commonly used for coin-cell electrodes. The simulations where the thickness of each electrode is different are to see if the model is capable of capturing the impact

that such difference has on performance in real-world application, as it is uncommon for both electrodes to be the exact same size in practice. It is known [91] that with increase in thickness of the electrodes there's an increase of capacity up to a point, due to more active material being present, however, the capacity of the cell begins to fall rapidly due to slower Li-ion diffusion caused by an increase in diffusion pathways. The power density also falls. Poor balancing in the thickness of the electrolytes can cause issues as well. For instance, a disproportionally thicker anode can cause lithium plating, which reduces the cycle life of the battery. On the contrary, a too thin anode can lead to the formation of dendrites, particularly at high C-rates. Long-term cycling behaviour is also affected negatively by large electrode thickness, with notable capacity fading due to mechanical issues and severe polarization.

Before this work could be started, it was necessary to add LFP to *Fluent's* material database, as it is not part of it by default, as mentioned previously. Obtaining the necessary parameters proved challenging. Obtaining the OCP curve for lithium was particularly hard, as it's rarely reported or estimated in the literature. The sources for each of the parameters used can be consulted in Appendix 6.

5. Results and Discussion

In this section, the results obtained from the simulation work conducted will be presented and discussed. The structure will follow the one in the previous chapter, beginning with the model validation followed by the thickness variation study. This order aligns roughly with how the work proceeded during the internship, but some results were obtained at a later date due to technical issues. This chapter will also not go over a great deal of work that, while essential, did not wield useful results.

5.1. Model validation

The model validation for an NMC half-cell was partially successful for a C-rate of 1.

The current value applied to the half-cell was 0.15 mA, while the average value of the current for the simulation was 0.44 mA, which is off by a factor of 3. The capacity for the cell was calculated from the current values, using equation 4.15, to be 0.39 mAh, while the experimental value was of 0.13 mAh. While the values are within the same order of magnitude, the calculated capacity is also off by a factor of 3.

As for the average voltage measured at the half-cell terminals, the value was 3.77 V while the simulated voltage average was 3.92 V. This corresponds to a relative error of, approximately, 3.9%. The discharge curve obtained through the simulation can be seen in figure 5.1 and the thermal behaviour of the half-cell in figure 5.2. Additionally, a picture of the geometry used with the mesh evident can be seen in figure 5.3 The significant difference between the experimental and simulated current indicates that issues exist within the half-cell model.

While there are many possible explanations for such a large error exist, among them, two seem particularly plausible.

The P2D model is particularly sensitive to change in parameters, with even small differences having the potential to cause very large changes in the simulation. As mentioned in the previous chapter, *Ansys Fluent* did not have metallic lithium as an option in its database, and this material had to be added manually to allow for the simulation of a half-cell. There's the possibility that the parameters of the metallic Lithium added are incorrect or dissonant with each other, as they were taken from different sources, thus explaining the current and capacity values obtained.

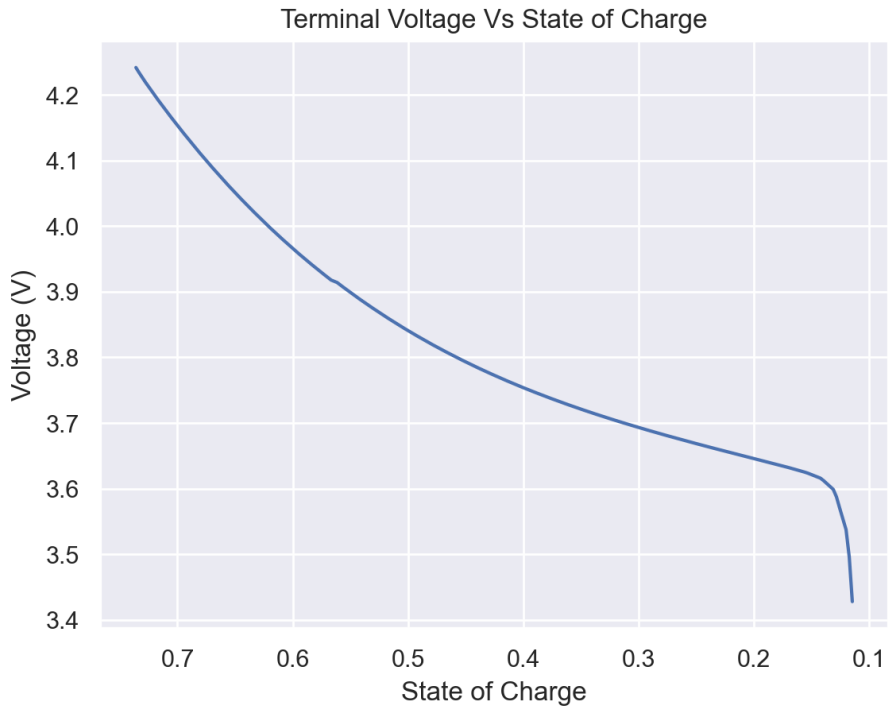

Figure 5.1: Discharge curve of the NMC validation cell

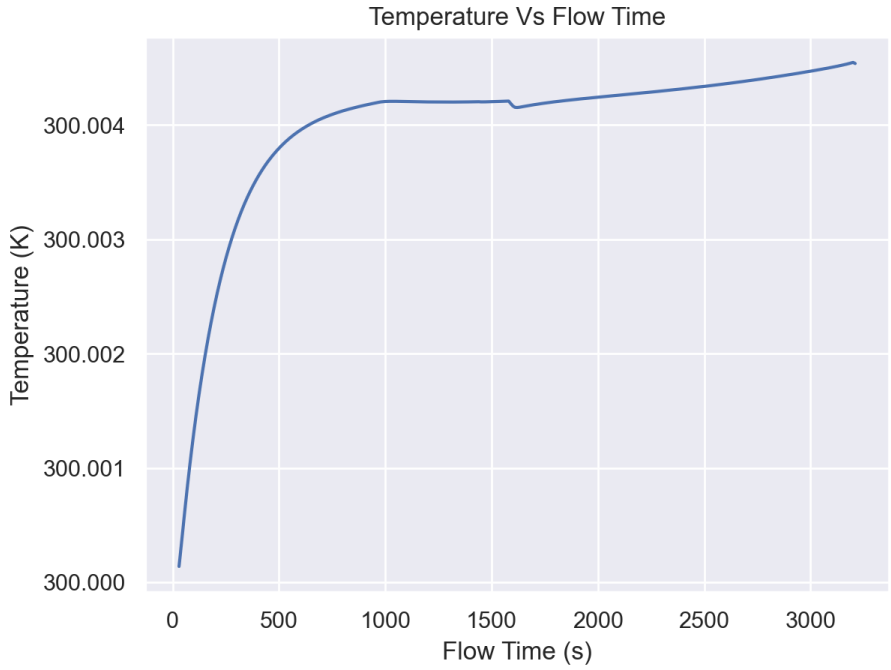

Figure 5.2: Battery maximum temperature as a function of time

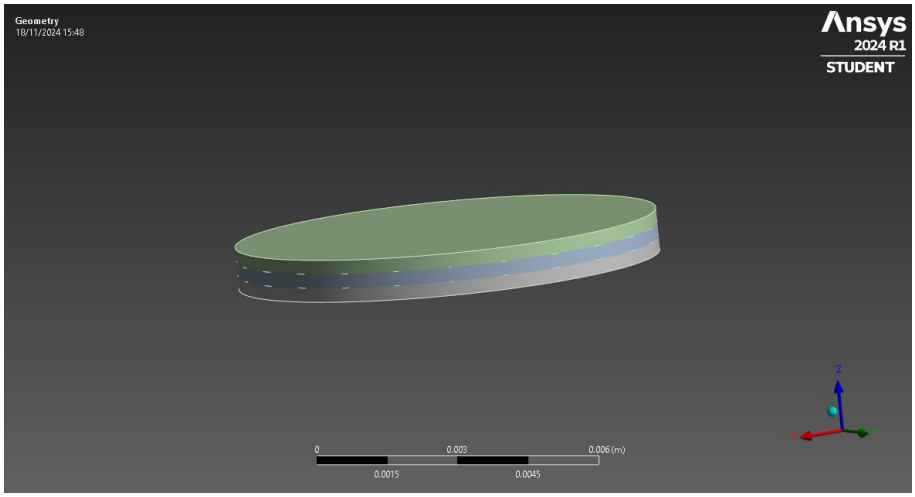

Figure 5.3: Picture of the geometry used for the validation. The top and bottom regions at the negative and positive current collector zones respectively, and the middle zone represents the active zone.

Alternatively, the explanation might lie in the thickness used. The thickness of both electrodes and the separator is of particular importance in the *Fluent's* implementation of the P2D model, as it is used by the software to provide a theoretical capacity per m^2, that is then used to estimate the capacity of the cell. This estimate serves as the nominal cell capacity for the electrical parameters of the battery model, which serves as the initial condition for the simulation. Therefore, if the thickness of any of the regions is incorrect, this has an even bigger impact in the simulation results than other parameters. The values for thickness of the electrodes and separator were taken from [90] as previously mentioned. However, it's possible that the values reported there are not of the electrodes and separator by themselves, but also include the positive and negative current collectors, or perhaps a substrate layer that is often used in experimental work. This additional thickness, while relatively small, might account for the large difference between the experimental and simulated values.

Overall, while far from ideal, the results obtained are within the order of magnitude of the experimental ones, with the voltage having a relatively low error. Furthermore, the shape of the different discharge curves are all in agreement to what is expected to be seen experimentally, consequently, the model partially fulfils the objective for which it was created.

The thermal profile of the validation cell is presented in figure 5.2. The overall behaviour is as expected, with an increase when the battery discharge process begins and then a slow increase with operation time. The absolute magnitude of the variation is small, which is

also to be expected given the small dimensions of the cell. At around 1600 seconds there's a small dip. This is likely due to some convergence error and is of no relevance to the overall simulation.

Additional simulations at different C-rates, that would account for the repeated cycling of the cell, were planned. However, due to immense technical difficulties and time constraints, this was not possible to do.

5.2. Thickness variation analysis

As described in chapter 4, the simulations conducted in the thickness variation analysis consist of two distinct groups: 4 in which both electrodes had the same thickness and a pair where the thickness of the positive and negative electrolyte differ. All simulations are of discharge cycles.

The capacities obtained for the different batteries can be consulted in table 5.4.

We can observe that there's an increase in capacity with an increase with electrode thickness. This is to be expected and is in agreement to what is observed experimentally. It is interesting to note that the battery with a negative electrode of 2×10^{-5} m and a positive one of 2×10^{-5} m outperforms the battery with converse dimensions, showing a higher capacity by about 6 %. Given that the anode is usually thicker in practical batteries, this is a positive indicator that the model can be of use for its intended purpose.

Cathode/Anode (m)	5x10^{-6}	1x10^{-5}	2x10^{-5}	2x10^{-5}
5x10^{-6}	1,742x10^{-4}			
1x10^{-5}		3,515x10^{-4}	3,610x10^{-4}	
2x10^{-5}		3,40x10^{-4}	7,077x10^{-4}	
3x10^{-5}				1,429x10^{-3}

Figure 5.4: Cell capacities (Ah) in function of the cathode and anode thickness.

To further analyse the impact of electrode thickness on battery performance, the discharge plot of the different batteries simulated are presented in figure 5.5.

From the graph presented in figure 5.5, several things are of interest. Firstly, the shape of all the discharge curves is as expected from experimental results. Indeed, there's a slight drop in voltage at the beginning of the discharge process, proceed by a slow decay until finally there's a sharp drop when the cells are nearly fully out of charge.

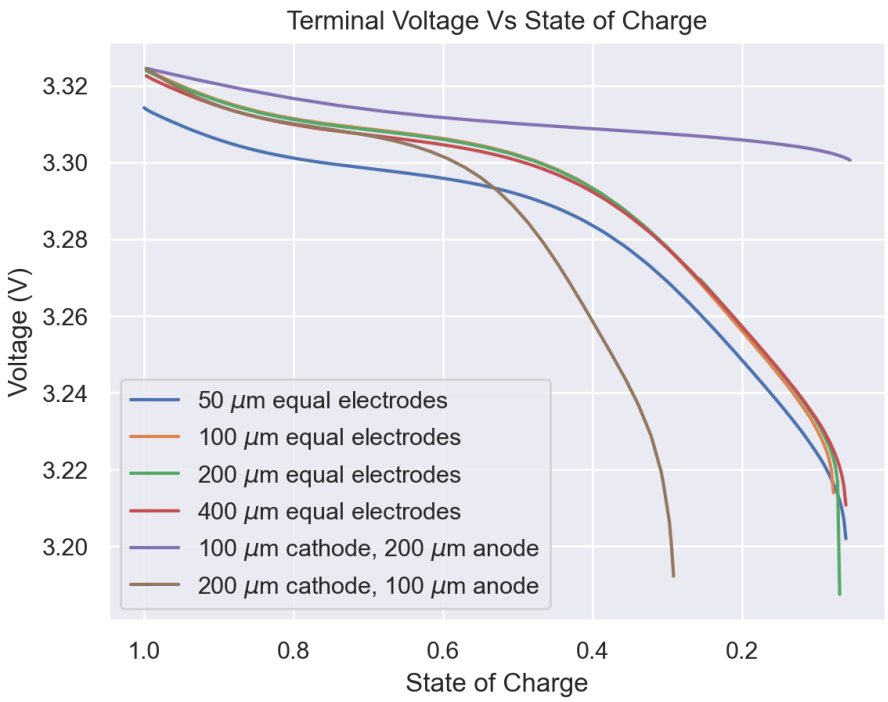

Figure 5.5: Discharge curves for the several batteries simulated.

No battery was able to discharge completely, the maximum SoC achieved being of around 3 %. This is to be expected, and is observed with batteries in real life measurements. In the simulation, this occurs because as the battery is near depletion, the equations for the Li-ion flow and continuity become increasingly hard to solve as the values approach zero, thus, the model eventually fails to converge. In fact, many simulation attempts crash entirely when this happens, as the software gets stuck trying to compute negative values for voltage and current.

The simulation of the battery with a thicker cathode and thinner anode fails to discharge past 30 %. The simulation parameters besides thickness were kept constant and several simulation attempts were made, however, the result was the same. It was assumed, then, that this indicates that a ratio of cathode to anode thickness above 1, negatively impacts battery performance. Ideally, this result would be confirmed with fabrication of a LFP battery in these conditions.

In figure 5.6, we can again see that, while the shape of the SoC curve is correct for all simulated cells, for the aforementioned battery with thicker cathode than anode, it stops at around 30 %.

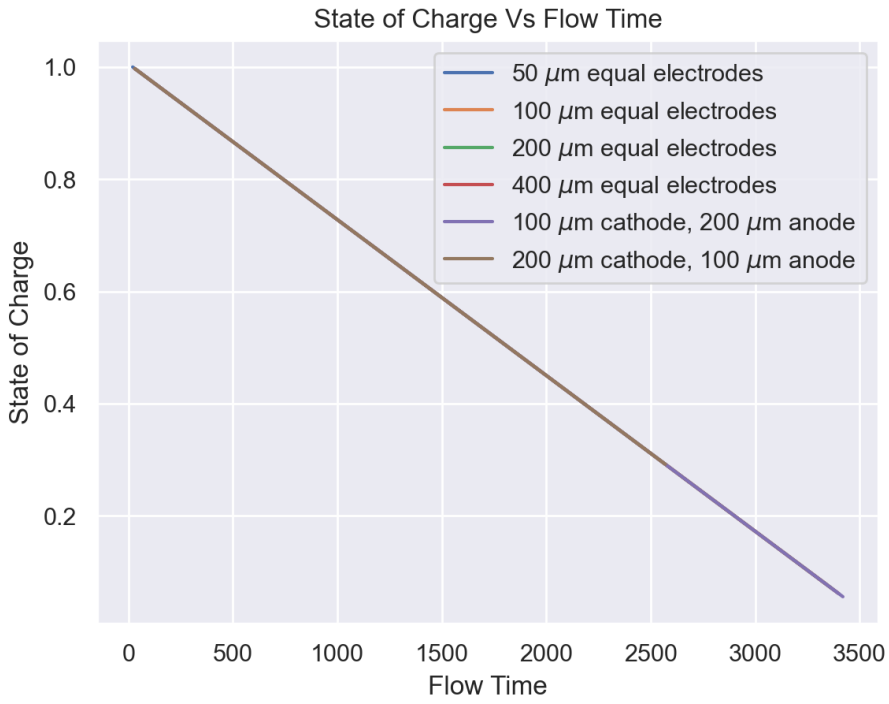

Figure 5.6: State of Charge in function of time for the several batteries simulated.

6. Conclusions and Future perspectives

6.1. Conclusions

The core objective of this work, that is, the development of a computational LFP battery model for simulation work was fulfilled. The model developed over the course of this project works and was successfully used to analyse the impact of electrode thickness on battery performance.

The beginning of this thesis involved a great deal of research on the operating principles of Li-ion batteries. Afterwards, an exploration of LFP as a cathode material was conducted and of several different numerical methods for simulation. The aggregate knowledge from the study of both the electrochemical and structural properties of Li-ion batteries and LFP as a cathode material, combined with the theoretical fundamentals behind the modelling of such devices allowed for a greater insight into the limitations of the numerical model that was later created, and to help explain the differences between the experimental results and the simulated ones.

The thorough state-of-the-art review that was done on both the experimental and computational modelling avenues for optimization of LFP cathodes granted a broad perspective on the different emerging areas within this research niche that might be of interest for an eventual future work.

Similar, although less thorough, work was also conducted for NMC batteries, including extensive simulation work with this cathode material. Indeed, a large portion of the testing phase was conducted using an NCM half-cell.

The development of the battery model was very challenging. Getting familiar with the *Ansys Workbench* suite and, in particular, with *Ansys Fluent* where the model itself was developed, was a slow and methodical process, with many setbacks along the way.

The model itself, while functional, is not as reliable nor as accurate as was intended when this project was started, having much room for improvement. However, it is a promising start and can already be of use to aid in experimental development of NMC and LFP batteries, even if only in an unpolished way.

6.2. Future Work

While the core objective of this project was accomplished, there's still much to do. To start, a more thorough validation of the model is in order, optimizing different parameters and possibly the geometry to better reflect experimental data and provide a better basis for experimental work.

The next step would be validating the model with an LFP cathode rather than an NMC one, because, although, validating with a different material is theoretically sound, it is not ideal.

Thinking even further ahead, synthesizing an LFP half-cell and full-cell for validation would be very interesting, as it would add an experimental component to the pure computational work done thus far, and allow for the application of a number of skills that were developed during the past two years. Indeed, this was initially presented as a possibly to be done during this project, but unfortunately, time was a limiting factor.

To conclude, exploring other platforms for simulation and perhaps other physics-based models to conduct a comparative study could also be of interest.

References

[1] N. O. Kapustin and D. A. Grushevenko, “Long-term electric vehicles outlook and their potential impact on electric grid,” *Energy Policy*, vol. 137, p. 111103, 2020. [Cited on page 1.]

[2] M. Muratori, M. Alexander, D. Arent, M. Bazilian, P. Cazzola, E. M. Dede, J. Farrell, C. Gearhart, D. Greene, A. Jenn *et al.*, “The rise of electric vehicles—2020 status and future expectations,” *Progress in Energy*, vol. 3, no. 2, p. 022002, 2021. [Cited on page 1.]

[3] M. Armand, P. Axmann, D. Bresser, M. Copley, K. Edström, C. Ekberg, D. Guyomard, B. Lestriez, P. Novák, M. Petranikova *et al.*, “Lithium-ion batteries–current state of the art and anticipated developments,” *Journal of Power Sources*, vol. 479, p. 228708, 2020. [Cited on page 1.]

[4] CeNTI - ”About Us: Welcome to CeNTI” (accessed 5th August 2024. [Cited on page 2.]

[5] B. Scrosati, “History of lithium batteries,” *Journal of solid state electrochemistry*, vol. 15, no. 7, pp. 1623–1630, 2011. [Cited on page 3.]

[6] T. Nagura and K. Tazawa, “Prog. batteries sol. cells,” *Batteries Sol. Cells*, vol. 9, p. 20, 1990. [Cited on page 3.]

[7] Let’s Talk Science - ”How does a lithium-Ion battery work?” (accessed 17th June 2024. [Cited on pages viii and 4.]

[8] Z. Ahsan, B. Ding, Z. Cai, C. Wen, W. Yang, Y. Ma, S. Zhang, G. Song, and M. S. Javed, “Recent progress in capacity enhancement of lifepo4 cathode for li-ion batteries,” *Journal of Electrochemical Energy Conversion and Storage*, vol. 18, no. 1, p. 010801, 2021. [Cited on pages 4 and 5.]

[9] J.-M. Tarascon and M. Armand, “Issues and challenges facing rechargeable lithium batteries,” *nature*, vol. 414, no. 6861, pp. 359–367, 2001. [Cited on pages viii and 5.]

[10] S. Lee and S. S. Park, “Atomistic simulation study of mixed-metal oxide (lini1/3co1/3mn1/3o2) cathode material for lithium ion battery,” *The Journal of Physical Chemistry C*, vol. 116, no. 10, pp. 6484–6489, 2012. [Cited on page 5.]

[11] M. Kuenzel, R. Porhiel, D. Bresser, J. Asenbauer, P. Axmann, M. Wohlfahrt-Mehrens, and S. Passerini, “Deriving structure-performance relations of chemically modified chitosan binders for sustainable high-voltage lini0. 5mn1. 5o4 cathodes,” *Batteries & Supercaps*, vol. 3, no. 2, pp. 155–164, 2020. [Cited on page 5.]

[12] L. Li, L. Wu, F. Wu, S. Song, X. Zhang, C. Fu, D. Yuan, and Y. Xiang, “recent research progress in surface modification of lifepo4 cathode materials,” *Journal of the Electrochemical Society*, vol. 164, no. 9, p. A2138, 2017. [Cited on page 5.]

[13] J. Wang and X. Sun, “Understanding and recent development of carbon coating on lifepo 4 cathode materials for lithium-ion batteries,” *Energy & Environmental Science*, vol. 5, no. 1, pp. 5163–5185, 2012. [Cited on page 5.]

[14] H. Fang, Z. Pan, L. Li, Y. Yang, G. Yan, G. Li, and S. Wei, “The possibility of manganese disorder in limnpo4 and its effect on the electrochemical activity,” *Electrochemistry communications*, vol. 10, no. 7, pp. 1071–1073, 2008. [Cited on page 5.]

[15] S. Rizvi, M. W. Tahir, N. Ramzan, and C. Merten, “Multiscale-multidomain model order reduction of lithium-ion batteries for automobile application: A review,” *Journal of Energy Storage*, vol. 99, p. 113390, 2024. [Cited on page 6.]

[16] M. Doyle, T. F. Fuller, and J. Newman, “Modeling of galvanostatic charge and discharge of the lithium/polymer/insertion cell,” *Journal of the Electrochemical society*, vol. 140, no. 6, p. 1526, 1993. [Cited on page 6.]

[17] T. F. Fuller, M. Doyle, and J. Newman, “Simulation and optimization of the dual lithium ion insertion cell,” *Journal of the electrochemical society*, vol. 141, no. 1, p. 1, 1994. [Cited on page 6.]

[18] M. Doyle, J. Newman, A. S. Gozdz, C. N. Schmutz, and J.-M. Tarascon, “Comparison of modeling predictions with experimental data from plastic lithium ion cells,” *Journal of the Electrochemical Society*, vol. 143, no. 6, p. 1890, 1996.

[19] K. Smith and C.-Y. Wang, “Solid-state diffusion limitations on pulse operation of a lithium ion cell for hybrid electric vehicles,” *Journal of power sources*, vol. 161, no. 1, pp. 628–639, 2006.

[20] L. Cai and R. E. White, “Reduction of model order based on proper orthogonal decomposition for lithium-ion battery simulations,” *Journal of the Electrochemical Society*, vol. 156, no. 3, p. A154, 2008.

[21] W. Lai and F. Ciucci, “Mathematical modeling of porous battery electrodes—revisit of newman’s model,” *Electrochimica Acta*, vol. 56, no. 11, pp. 4369–4377, 2011. [Cited on page 6.]

[22] T.-S. Dao, C. P. Vyasarayani, and J. McPhee, “Simplification and order reduction of lithium-ion battery model based on porous-electrode theory,” *Journal of Power Sources*, vol. 198, pp. 329–337, 2012. [Cited on pages 6 and 7.]

[23] J. Newman and W. Tiedemann, “Porous-electrode theory with battery applications,” *AIChE Journal*, vol. 21, no. 1, pp. 25–41, 1975. [Cited on page 6.]

[24] J. Newman and N. P. Balsara, *Electrochemical systems*. John Wiley & Sons, 2021. [Cited on page 8.]

[25] A. A. Franco, “Multiscale modelling and numerical simulation of rechargeable lithium ion batteries: concepts, methods and challenges,” *Rsc Advances*, vol. 3, no. 32, pp. 13 027–13 058, 2013. [Cited on page 9.]

[26] G. K. P. Dathar, D. Sheppard, K. J. Stevenson, and G. Henkelman, “Calculations of li-ion diffusion in olivine phosphates,” *Chemistry of Materials*, vol. 23, no. 17, pp. 4032–4037, 2011. [Cited on page 11.]

[27] M. S. Islam, D. J. Driscoll, C. A. Fisher, and P. R. Slater, “Atomic-scale investigation of defects, dopants, and lithium transport in the lifepo4 olivine-type battery material,” *Chemistry of Materials*, vol. 17, no. 20, pp. 5085–5092, 2005. [Cited on page 11.]

[28] J. Su, X.-L. Wu, C.-P. Yang, J.-S. Lee, J. Kim, and Y.-G. Guo, “Self-assembled lifepo4/c nano/microspheres by using phytic acid as phosphorus source,” *The Journal of Physical Chemistry C*, vol. 116, no. 8, pp. 5019–5024, 2012. [Cited on page 11.]

[29] M. Chen, X. Wang, H. Shu, R. Yu, X. Yang, and W. Huang, “Solvothermal synthesis of monodisperse micro-nanostructure starfish-like porous lifepo4 as cathode material for lithium-ion batteries,” *Journal of Alloys and Compounds*, vol. 652, pp. 213–219, 2015. [Cited on page 11.]

[30] Z. Zheng, W. K. Pang, X. Tang, D. Jia, Y. Huang, and Z. Guo, “Solvothermal synthesis and electrochemical performance of hollow lifepo4 nanoparticles,” *Journal of Alloys and Compounds*, vol. 640, pp. 95–100, 2015. [Cited on page 12.]

[31] S. Yang, M. Hu, L. Xi, R. Ma, Y. Dong, and C. Chung, “Solvothermal synthesis of monodisperse lifepo4 micro hollow spheres as high performance cathode material for lithium ion batteries,” *ACS applied materials & interfaces*, vol. 5, no. 18, pp. 8961–8967, 2013. [Cited on pages 12 and 20.]

[32] Y. Zhao, L. Peng, B. Liu, and G. Yu, “Single-crystalline lifepo4 nanosheets for high-rate li-ion batteries,” *Nano letters*, vol. 14, no. 5, pp. 2849–2853, 2014. [Cited on page 12.]

[33] X. Huang, X. He, C. Jiang, and G. Tian, “Morphology evolution and impurity analysis of lifepo 4 nanoparticles via a solvothermal synthesis process,” *Rsc Advances*, vol. 4, no. 99, pp. 56 074–56 083, 2014. [Cited on page 12.]

[34] Z. Li, Z. Peng, H. Zhang, T. Hu, M. Hu, K. Zhu, and X. Wang, “[100]-oriented lifepo4 nanoflakes toward high rate li-ion battery cathode,” *Nano letters*, vol. 16, no. 1, pp. 795–799, 2016. [Cited on page 12.]

[35] X. Huang, Y. Yao, F. Liang, and Y. Dai, “Concentration-controlled morphology of lifepo4 crystals with an exposed (100) facet and their enhanced performance for use in lithium-ion batteries,” *Journal of Alloys and Compounds*, vol. 743, pp. 763–772, 2018. [Cited on page 12.]

[36] Z. Ma, G. Shao, Y. Fan, G. Wang, J. Song, and T. Liu, “Tunable morphology synthesis of lifepo4 nanoparticles as cathode materials for lithium ion batteries,” *ACS Applied Materials & Interfaces*, vol. 6, no. 12, pp. 9236–9244, 2014. [Cited on page 13.]

[37] O. Xiuqin, P. Lin, G. Haichen, W. Yichen, and L. Jianwei, “Temperature-dependent crystallinity and morphology of lifepo 4 prepared by hydrothermal synthesis,” *Journal of Materials Chemistry*, vol. 22, no. 18, pp. 9064–9068, 2012. [Cited on page 13.]

[38] X. Huang, X. He, C. Jiang, G. Tian, and Y. Liu, “Reaction mechanisms on solvothermal synthesis of nano lifepo4 crystals and defect analysis,” *Industrial & Engineering Chemistry Research*, vol. 56, no. 38, pp. 10 648–10 657, 2017. [Cited on page 13.]

[39] S. Dhaybi, B. Marsan, and A. Hammami, “A novel low-cost and simple colloidal route for preparing high-performance carbon-coated lifepo4 for lithium batteries,” *Journal of Energy Storage*, vol. 18, pp. 259–265, 2018. [Cited on page 13.]

[40] M. Cuisinier, N. Dupré, P. Moreau, and D. Guyomard, “Nmr monitoring of electrode/-electrolyte interphase in the case of air-exposed and carbon coated lifepo4,” *Journal of power sources*, vol. 243, pp. 682–690, 2013. [Cited on page 14.]

[41] H. Liu, C. Li, H. Zhang, L. Fu, Y. Wu, and H. Wu, “Kinetic study on lifepo4/c nanocomposites synthesized by solid state technique,” *Journal of Power Sources*, vol. 159, no. 1, pp. 717–720, 2006. [Cited on page 14.]

[42] Q.-B. Liu, S.-J. Liao, H.-Y. Song, and Z.-X. Liang, “High-performance lifepo4/c materials: Effect of carbon source on microstructure and performance,” *Journal of Power Sources*, vol. 211, pp. 52–58, 2012. [Cited on page 14.]

[43] M. Mollazadeh and B. Habibi, “Lifepo 4/carbon/reduced graphene oxide nanostructured composite as a high capacity and fast rate cathode material for rechargeable lithium ion battery,” *Catalysis Letters*, vol. 149, pp. 7–18, 2019. [Cited on page 14.]

[44] H. Raj and A. Sil, “Effect of carbon coating on electrochemical performance of lifepo 4 cathode material for li-ion battery,” *Ionics*, vol. 24, pp. 2543–2553, 2018. [Cited on page 14.]

[45] Y. Rao, K. Wang, and H. Zeng, “The effect of phenol–formaldehyde resin on the electrochemical properties of carbon-coated lifepo4 materials in pilot scale,” *Ionics*, vol. 21, no. 6, pp. 1525–1531, 2015.

[46] A. R. Iarchuk, V. A. Nikitina, E. A. Karpushkin, V. G. Sergeyev, E. V. Antipov, K. J. Stevenson, and A. M. Abakumov, “Influence of carbon coating on intercalation kinetics and transport properties of lifepo4,” *ChemElectroChem*, vol. 6, no. 19, pp. 5090–5100, 2019. [Cited on page 14.]

[47] N. Liu, M. Gao, Z. Li, C. Li, W. Wang, H. Zhang, Z. Yu, and Y. Huang, “Effect of gelatin concentration on the synthetize of the lifepo4/c composite for lithium ion batteries,” *Journal of alloys and compounds*, vol. 599, pp. 127–130, 2014. [Cited on page 14.]

[48] Y. Wang, R. Mei, and X. Yang, “Enhanced electrochemical properties of lifepo4/c synthesized with two kinds of carbon sources, peg-4000 (organic) and super p (inorganic),” *Ceramics International*, vol. 40, no. 6, pp. 8439–8444, 2014.

[49] Y. Meng, J. Xia, L. Wang, G. Wang, F. Zhu, and Y. Zhang, “A comparative study on lifepo4/c by in-situ coating with different carbon sources for high-performance lithium

batteries," *Electrochimica Acta*, vol. 261, pp. 96–103, 2018. [Cited on pages 14 and 16.]

[50] B. Ding, G. Ji, Z. Sha, J. Wu, L. Lu, and J. Y. Lee, "Dual-carbon network for the effective transport of charged species in a lifepo4 cathode for lithium-ion batteries," *Energy Technology*, vol. 3, no. 1, pp. 63–69, 2015. [Cited on page 14.]

[51] G. Jiang, Z. Hu, J. Xiong, X. Zhu, and S. Yuan, "Enhanced performance of lifepo4 originating from the synergistic effect of graphene modification and carbon coating," *Journal of Alloys and Compounds*, vol. 767, pp. 528–537, 2018. [Cited on page 15.]

[52] J. Oh, J. Lee, T. Hwang, J. M. Kim, K.-d. Seoung, and Y. Piao, "Dual layer coating strategy utilizing n-doped carbon and reduced graphene oxide for high-performance lifepo4 cathode material," *Electrochimica Acta*, vol. 231, pp. 85–93, 2017. [Cited on page 15.]

[53] J. Wang, Y.-J. Gu, W.-L. Kong, H.-Q. Liu, Y.-B. Chen, and W. Liu, "Effect of carbon coating on the crystal orientation and electrochemical performance of nanocrystalline lifepo4," *Solid State Ionics*, vol. 327, pp. 11–17, 2018. [Cited on page 16.]

[54] Y. Guan, J. Shen, X. Wei, Q. Zhu, X. Zheng, S. Zhou, and B. Xu, "Lifepo4/activated carbon/graphene composite with capacitive-battery characteristics for superior high-rate lithium-ion storage," *Electrochimica Acta*, vol. 294, pp. 148–155, 2019. [Cited on page 16.]

[55] Z. Cao, G. Zhu, R. Zhang, S. Chen, M. Sang, J. Jia, M. Yang, X. Li, and S. Yang, "Biological phytic acid guided formation of monodisperse large-sized carbon@ lifepo4/graphene composite microspheres for high-performance lithium-ion battery cathodes," *Chemical Engineering Journal*, vol. 351, pp. 382–390, 2018. [Cited on page 17.]

[56] B. Lung-Hao Hu, F.-Y. Wu, C.-T. Lin, A. N. Khlobystov, and L.-J. Li, "Graphene-modified lifepo4 cathode for lithium ion battery beyond theoretical capacity," *Nature communications*, vol. 4, no. 1, p. 1687, 2013. [Cited on page 17.]

[57] Q. Zhao, Y. Zhang, Y. Meng, Y. Wang, J. Ou, Y. Guo, and D. Xiao, "Phytic acid derived lifepo4 beyond theoretical capacity as high-energy density cathode for lithium ion battery," *Nano Energy*, vol. 34, pp. 408–420, 2017. [Cited on page 17.]

[58] Z. Jinli, W. Jiao, L. Yuanyuan, N. Ning, G. Junjie, Y. Feng, and L. Wei, "High-performance lithium iron phosphate with phosphorus-doped carbon layers for lithium ion batteries," *Journal of Materials Chemistry A*, vol. 3, no. 5, pp. 2043–2049, 2015. [Cited on page 18.]

[59] J. Feng and Y. Wang, "High-rate and ultralong cycle-life lifepo4 nanocrystals coated by boron-doped carbon as positive electrode for lithium-ion batteries," *Applied Surface Science*, vol. 390, pp. 481–488, 2016. [Cited on page 18.]

[60] X. Wang, Z. Feng, X. Hou, L. Liu, M. He, X. He, J. Huang, and Z. Wen, "Fluorine doped carbon coating of lifepo4 as a cathode material for lithium-ion batteries," *Chemical Engineering Journal*, vol. 379, p. 122371, 2020. [Cited on page 18.]

[61] B. Han, X. Meng, L. Ma, and J. Nan, "Nitrogen-doped carbon decorated lifepo4 composite synthesized via a microwave heating route using polydopamine as carbon–nitrogen precursor," *Ceramics International*, vol. 42, no. 2, pp. 2789–2797, 2016. [Cited on page 19.]

[62] Q. Xiong, J. Lou, X. Teng, X. Lu, S. Liu, H. Chi, and Z. Ji, "Controllable synthesis of nc@ lifepo4 nanospheres as advanced cathode of lithium ion batteries," *Journal of Alloys and Compounds*, vol. 743, pp. 377–382, 2018. [Cited on page 19.]

[63] J. Zhang, N. Nie, Y. Liu, J. Wang, F. Yu, J. Gu, and W. Li, "Boron and nitrogen codoped carbon layers of lifepo4 improve the high-rate electrochemical performance for lithium ion batteries," *ACS applied materials & interfaces*, vol. 7, no. 36, pp. 20 134–20 143, 2015. [Cited on page 19.]

[64] S.-X. Zhao, H. Ding, Y.-C. Wang, B.-H. Li, and C.-W. Nan, "Improving rate performance of lifepo4 cathode materials by hybrid coating of nano-li3po4 and carbon," *Journal of Alloys and Compounds*, vol. 566, pp. 206–211, 2013. [Cited on page 20.]

[65] H. Shu, M. Chen, Y. Fu, X. Yang, X. Yi, Y. Bai, Q. Liang, Q. Wei, B. Hu, J. Tan *et al.*, "Improvement of electrochemical performance for spherical lifepo4 via hybrid coated with electron conductive carbon and fast li ion conductive la0. 56li0. 33tio3," *Journal of Power Sources*, vol. 252, pp. 73–78, 2014. [Cited on page 20.]

[66] S.-Y. Chung and Y.-M. Chiang, "Microscale measurements of the electrical conductivity of doped lifepo4," *Electrochemical and solid-state letters*, vol. 6, no. 12, p. A278, 2003. [Cited on page 21.]

[67] I. D. Johnson, E. Blagovidova, P. A. Dingwall, D. J. Brett, P. R. Shearing, and J. A. Darr, “High power nb-doped lifepo4 li-ion battery cathodes; pilot-scale synthesis and electrochemical properties,” *Journal of Power Sources*, vol. 326, pp. 476–481, 2016. [Cited on page 21.]

[68] C.-Y. Chiang, H.-C. Su, P.-J. Wu, H.-J. Liu, C.-W. Hu, N. Sharma, V. K. Peterson, H.-W. Hsieh, Y.-F. Lin, W.-C. Chou *et al.*, “Vanadium substitution of lifepo4 cathode materials to enhance the capacity of lifepo4-based lithium-ion batteries,” *The Journal of Physical Chemistry C*, vol. 116, no. 46, pp. 24 424–24 429, 2012. [Cited on page 21.]

[69] M. Wagemaker, B. L. Ellis, D. Lutzenkirchen-Hecht, F. M. Mulder, and L. F. Nazar, “Proof of supervalent doping in olivine lifepo4,” *Chemistry of Materials*, vol. 20, no. 20, pp. 6313–6315, 2008. [Cited on page 21.]

[70] J. Barker, M. Saidi, and J. Swoyer, “Lithium iron (ii) phospho-olivines prepared by a novel carbothermal reduction method,” *Electrochemical and Solid-State Letters*, vol. 6, no. 3, p. A53, 2003. [Cited on page 21.]

[71] B. Wang, B. Xu, T. Liu, P. Liu, C. Guo, S. Wang, Q. Wang, Z. Xiong, D. Wang, and X. Zhao, “Mesoporous carbon-coated lifepo 4 nanocrystals co-modified with graphene and mg 2+ doping as superior cathode materials for lithium ion batteries,” *Nanoscale*, vol. 6, no. 2, pp. 986–995, 2014. [Cited on page 21.]

[72] A. Örnek and O. Efe, “Doping qualifications of life1- xmgxpo4-c nano-scale composite cathode materials,” *Electrochimica Acta*, vol. 166, pp. 338–349, 2015. [Cited on page 21.]

[73] I. D. Johnson, M. Lübke, O. Y. Wu, N. M. Makwana, G. J. Smales, H. U. Islam, R. Y. Dedigama, R. I. Gruar, C. J. Tighe, D. O. Scanlon *et al.*, “Pilot-scale continuous synthesis of a vanadium-doped lifepo4/c nanocomposite high-rate cathodes for lithium-ion batteries,” *Journal of Power Sources*, vol. 302, pp. 410–418, 2016. [Cited on page 22.]

[74] S. Jiang and Y. Wang, “Synthesis and characterization of vanadium-doped lifepo4@ c electrode with excellent rate capability for lithium-ion batteries,” *Solid State Ionics*, vol. 335, pp. 97–102, 2019. [Cited on page 22.]

[75] A. Örnek, E. Bulut, M. Can, and M. Özacar, “Characteristics of nanosized lini x fe 1- x po 4/c (x= 0.00–0.20) composite material prepared via sol–gel-assisted carbothermal

reduction method," *Journal of Solid State Electrochemistry*, vol. 17, pp. 3101–3107, 2013. [Cited on page 22.]

[76] D. Zhang, J. Wang, K. Dong, and A. Hao, "First principles investigation on the elastic and electronic properties of mn, co, nb, mo doped lifepo4," *Computational Materials Science*, vol. 155, pp. 410–415, 2018. [Cited on page 22.]

[77] K. Okada, I. Kimura, and K. Machida, "High rate capability by sulfur-doping into lifepo 4 matrix," *RSC advances*, vol. 8, no. 11, pp. 5848–5853, 2018. [Cited on page 22.]

[78] C. Gao, J. Zhou, G. Liu, and L. Wang, "Synthesis of f-doped lifepo4/c cathode materials for high performance lithium-ion batteries using co-precipitation method with hydrofluoric acid source," *Journal of Alloys and Compounds*, vol. 727, pp. 501–513, 2017. [Cited on page 23.]

[79] X. Li, Z. Shao, K. Liu, Q. Zhao, G. Liu, and B. Xu, "Effect of f-doping on the properties of lifepo 4-x/3 f x/c cathode materials via wet mechanical agitation-assisted high-temperature ball milling method," *Journal of Solid State Electrochemistry*, vol. 22, pp. 2837–2843, 2018. [Cited on page 23.]

[80] J. Tu, K. Wu, H. Tang, H. Zhou, and S. Jiao, "Mg–ti co-doping behavior of porous lifepo 4 microspheres for high-rate lithium-ion batteries," *Journal of Materials Chemistry A*, vol. 5, no. 32, pp. 17 021–17 028, 2017. [Cited on page 23.]

[81] Z. Tian, Z. Zhou, S. Liu, F. Ye, and S. Yao, "Enhanced properties of olivine lifepo4/graphene co-doped with nb5+ and ti4+ by a sol–gel method," *Solid State Ionics*, vol. 278, pp. 186–191, 2015. [Cited on page 23.]

[82] D. Kong, G. Wang, P. Ping, and J. Wen, "Numerical investigation of thermal runaway behavior of lithium-ion batteries with different battery materials and heating conditions," *Applied Thermal Engineering*, vol. 189, p. 116661, 2021. [Cited on page 24.]

[83] M. Henriksen, K. Vaagsaether, J. Lundberg, S. Forseth, and D. Bjerketvedt, "Simulation of a premixed explosion of gas vented during li-ion battery failure," *Fire safety journal*, vol. 126, p. 103478, 2021. [Cited on page 24.]

[84] W. Zhao, G. Luo, and C.-Y. Wang, "Effect of tab design on large-format li-ion cell performance," *Journal of Power Sources*, vol. 257, pp. 70–79, 2014. [Cited on page 24.]

[85] A. Nazari, R. Esmaeeli, S. R. Hashemi, H. Aliniagerdroudbari, and S. Farhad, "The effect of temperature on lithium-ion battery energy efficiency with graphite/lifepo4

electrodes at different nominal capacities," in *Asme power conference*, vol. 51401. American Society of Mechanical Engineers, 2018, p. V002T09A008. [Cited on pages 24 and 60.]

[86] ——, "Low-temperature energy efficiency of lithium-ion batteries," in *ASME International Mechanical Engineering Congress and Exposition*, vol. 52071. American Society of Mechanical Engineers, 2018, p. V06AT08A026. [Cited on pages 25 and 60.]

[87] Y. Jiang, L. Zhang, G. Offer, and H. Wang, "A user-friendly lithium battery simulator based on open-source cfd," *Digital Chemical Engineering*, vol. 5, p. 100055, 2022. [Cited on page 26.]

[88] I. ANSYS, "Ansys fluent theory guide," *ANSYS Inc. URL http://www. ansys. com*, 2022. [Cited on pages 26 and 27.]

[89] ——, "Ansys fluent user's guide," *ANSYS Inc. URL http://www. ansys. com*, 2022. [Cited on pages 29, 32, and 34.]

[90] P. Sampaio, "Desenvolvimento de bateriais flexíveis sustentáveis para wearables," Master's thesis, University of Minho, 2023. [Cited on pages 38, 39, and 44.]

[91] H. Zheng, J. Li, X. Song, G. Liu, and V. S. Battaglia, "A comprehensive understanding of electrode thickness effects on the electrochemical performances of li-ion battery cathodes," *Electrochimica Acta*, vol. 71, pp. 258–265, 2012. [Cited on page 41.]

[92] J. Li, M. Zhao, C. Dai, Z. Wang, and M. Pecht, "A mathematical method for open-circuit potential curve acquisition for lithium-ion batteries," *Journal of Electroanalytical Chemistry*, vol. 895, p. 115488, 2021. [Cited on page 60.]

[93] C. Wang and J. Hong, "Ionic/electronic conducting characteristics of lifepo4 cathode materials: The determining factors for high rate performance," *Electrochemical and solid-state letters*, vol. 10, no. 3, p. A65, 2007.

[94] M. E. Ferraro, B. L. Trembacki, V. E. Brunini, D. R. Noble, and S. A. Roberts, "Electrode mesoscale as a collection of particles: coupled electrochemical and mechanical analysis of nmc cathodes," *Journal of The Electrochemical Society*, vol. 167, no. 1, p. 013543, 2020. [Cited on page 60.]

[95] Electrical Conductivity of the elements, (accessed 13th March 2024. [Cited on page 60.]

[96] Lithium, (accessed 17th March 2024. [Cited on page 60.]

Annex A:

The parameters used in the validation were obtained from several works [85, 86, 92–94] and other sources [95, 96] are presented below:

	Positive Electrode	References
Material Name	NCM-111	-
Thickness	$2x10^{-5}$	-
Number of Grids	10	*Fluent* defaul value
Grid Size Ratio	1	*Fluent* defaul value
Particle Diamter (m)	$1,6x10^{-5}$	*Fluent* defaul value
Number of Grids in Solid	15	*Fluent* defaul value
Grid Size Ratio in Solid	0.8	*Fluent* defaul value
Cs, max (mol/m^3)	22860	*Fluent* defaul value
Stoi. At 0% SOC	0.99	*Fluent* defaul value
Stoi. At 100% SOC	0.17	*Fluent* defaul value
Init.Cs (mol/m^3)	3886.2	*Fluent* defaul value
Init.Ce (mol/m^3)	2000	*Fluent* defaul value
VOF of Eletrolite	0.444	*Fluent* defaul value
Filler Fraction	0.259	*Fluent* defaul value
Ds,p (m^2/s)	$1x10^{-13}$	*Fluent* defaul value
Activation energy E_d (j/mol)	0	*Fluent* defaul value
Brugg_p	1.5	*Fluent* defaul value
Conductivity (S/m)	4.9	[94]
Ref. Rate Constant	$3.38x10^{-7}$	[93]
Activation energy E_r (j/mol)	0	*Fluent* defaul value
Trans. Coef. a	0.5	*Fluent* defaul value
Trans. Coef. C	0.5	*Fluent* defaul value
OCP_p (V)	piecewise-linear	*Fluent* defaul value

Figure 1: Parameters for the Positive electrode NCM-111

	Positive Electrode	References
Material Name	LFP	-
Thickness	$5x10^{-6}$	-
Number of Grids	10	*Fluent* defaul value
Grid Size Ratio	1	*Fluent* defaul value
Particle Diamter (m)	$1,6x10^{-5}$	*Fluent* defaul value
Number of Grids in Solid	15	*Fluent* defaul value
Grid Size Ratio in Solid	0.8	*Fluent* defaul value
Cs, max (mol/m^3)	22860	*Fluent* defaul value
Stoi. At 0% SOC	0.99	*Fluent* defaul value
Stoi. At 100% SOC	0.17	*Fluent* defaul value
Init.Cs (mol/m^3)	3886.2	*Fluent* defaul value
Init.Ce (mol/m^3)	2000	*Fluent* defaul value
VOF of Eletrolite	0.444	*Fluent* defaul value
Filler Fraction	0.259	*Fluent* defaul value
Ds,p (m^2/s)	$1x10^{-13}$	*Fluent* defaul value
Activation energy E_d (j/mol)	0	*Fluent* defaul value
Brugg_p	1.5	*Fluent* defaul value
Conductivity (S/m)	91	[85], [86]
Ref. Rate Constant	$5x10^{-10}$	[85], [86]
Activation energy E_r (j/mol)	0	*Fluent* defaul value
Trans. Coef. a	0.5	*Fluent* defaul value
Trans. Coef. C	0.5	*Fluent* defaul value
OCP_p (V)	piecewise-linear	[91]

Figure 2: Parameters for the Positive electrode LFP

	Negative Eletrode	References
Material Name	Lithium	-
Thickness	$3x10^{-5}$	-
Number of Grids	10	*Fluent* defaul value
Grid Size Ratio	1	*Fluent* defaul value
Particle Diamter (m)	$1x10^{-7}$	*Fluent* defaul value
Number of Grids in Solid	15	*Fluent* defaul value
Grid Size Ratio in Solid	0.8	*Fluent* defaul value
Cs, max (mol/m^3)	26390	*Fluent* defaul value
Stoi. At 0% SOC	0.005	*Fluent* defaul value
Stoi. At 100% SOC	0.5635	*Fluent* defaul value
Init.Cs (mol/m^3)	14870.76	*Fluent* defaul value
Init.Ce (mol/m^3)	2000	*Fluent* defaul value
VOF of Eletrolite	0.357	*Fluent* defaul value
Filler Fraction	0.172	*Fluent* defaul value
Ds,p (m^2/s)	$7,5x10^{-10}$	[95]
Activation energy E_d (j/mol)	0	*Fluent* defaul value
Brugg_n	1.5	*Fluent* defaul value
Conductivity (S/m)	$1,2x10^{7}$	[94]
Ref. Rate Constant	$2,5x10^{-13}$	[95]
Activation energy E_r (j/mol)	0	*Fluent* defaul value
Trans. Coef. a	0.5	*Fluent* defaul value
Trans. Coef. C	0.5	*Fluent* defaul value
OCP_n (V)	0	Theory

Figure 3: Parameters for the Negative electrode Lithium

	Negative Eletrode	References
Material Name	Graphite	-
Thickness	$5x10^{-6}$	-
Number of Grids	10	*Fluent* defaul value
Grid Size Ratio	1	*Fluent* defaul value
Particle Diamter (m)	$1x10^{-7}$	*Fluent* defaul value
Number of Grids in Solid	15	*Fluent* defaul value
Grid Size Ratio in Solid	0.8	*Fluent* defaul value
:s, max (mol/m^3)	26390	*Fluent* defaul value
Stoi. At 0% SOC	0.005	*Fluent* defaul value
Stoi. At 100% SOC	0.5635	*Fluent* defaul value
Init.Cs (mol/m^3)	14870.76	*Fluent* defaul value
Init.Ce (mol/m^3)	2000	*Fluent* defaul value
VOF of Eletrolite	0.357	*Fluent* defaul value
Filler Fraction	0.172	*Fluent* defaul value
Ds,p (m^2/s)	$3,9x10^{-14}$	[85], [86]
Activation energy E_d (j/mol)	0	*Fluent* defaul value
Brugg_n	1.5	*Fluent* defaul value
Conductivity (S/m)	100	[85], [86]
Ref. Rate Constant	$4,82x10^{-6}$	[85], [86]
Activation energy E_r (j/mol)	0	*Fluent* defaul value
Trans. Coef. a	0.5	*Fluent* defaul value
Trans. Coef. C	0.5	*Fluent* defaul value
OCP_n (V)	piecewise-linear	Fluent defaul value

Figure 4: Parameters for the Negative electrode Graphite

	Separator	References
Thickness	$5x10^{-6}$	-
Number of Grids	5	*Fluent* defaul value
Init.Ce (mol/m^3)	2000	*Fluent* defaul value
VOF of Eletrolite	1	*Fluent* defaul value
Brugg_s	1.5	*Fluent* defaul value

Figure 5: Parameters for the Separator

	Electrolyte	References
De (m^2/s)	$9x10^{-11}$	*Fluent* defaul value
t+ Factor	0.4	*Fluent* defaul value
Ionic Cond. (S/m)	polynomial	*Fluent* defaul value
Activity Term	0	*Fluent* defaul value

Figure 6: Parameters for the Electrolyte EC-DMC-LIPF6